The International Journal of Advanced Manufacturing Technology
https://doi.org/10.1007/s00170-026-17455-5

ORIGINAL ARTICLE

Effect of additional underneath magnetic field on joining mechanism of aluminum alloy to galvanized steel joints in pulsed current gas metal arc welding

Seong Min Hong[1] · Shinichi Tashiro[1] · Hee-Seon Bang[2] · Kenta Yamanaka[3] · Manabu Tanaka[1] · Kazuhiro Ito[1]

Received: 7 November 2025 / Accepted: 6 January 2026

Abstract
In joining of aluminum alloy to steel by pulsed current gas metal arc welding (GMAW) process, drastic input of heat energy from the arc heat source causes an excessive growth of brittle Fe-Al intermetallics layer and blow holes. In this study, application of additional underneath magnetic field (B) to GMAW was attempted to clarify the effect of controlled Lorentz force on heat input, joining mechanism, and Fe-Al IMC growth at the joint interface. 1.2 mm thick AA5052 aluminum alloy and hot-dip galvanized steel were joined in lap configuration by varying the B direction to control the Lorentz force. Arc phenomenon and weld pool flow, macroscopic and microscopic observation of the joints, and corresponding tensile-shear strength of the joints were investigated to understand the joining mechanism. It was found that the additional underneath Lorentz force to the rear side oscillated the arc to the steel side depending on the welding current and decreased the energy density to the base metal. Further, the Lorentz force transformed bead formation and suppressed IMC layer growth with showing the maximum tensile-shear strength as 187 MPa.

Keywords Pulsed current GMAW · Underneath additional magnetic field · Lorentz force · Aluminum alloy · Hot-dip galvanized steel · IMC layer

1 Introduction

It is known that the gas metal arc welding (GMAW) is still one of the challenging ways to join aluminum to steel due to the sensitive and complicated mechanism of the arc [1–3], but its high thermal efficiency with high joining speed in complex joint geometry is still attractive to be adopted in the dissimilar materials joining. Furthermore, huge gap of thermo-physical properties such as thermal conductivity, thermal expansion, and heat or the metallurgical difference like solid solubility and lattice transformation between the aluminum alloy and steel require the proper heat input to the joint interface to prevent deformation or defects such as blow hole, cracks, insufficient fusion, and excessive growth of brittle Fe-Al intermetallics (IMC) [4]. In fusion welding method, especially, the formation of Fe-Al IMC layer at the joint interface is inevitable but its highly brittle characteristics stands in need to control the growth of IMC layer to be less than 10 μm [5–7].

Therefore, many of research have been carried out to figure out the applicability of GMAW in joining of steel to aluminum alloy by investigating the growth mechanism of Fe-Al IMC, chemical compositions of supplementary mediums such as electrode filler wire, and coating or interlayer on the base metal. Based on the Fe-Al IMC layer is formed mainly by the melting pool temperature and time [8, 9], Wang et al. [10] found that the chemical reaction between Fe and Al requires lower enthalpy than Fe and Zn, or Al and Zn, so that the Fe-Al IMC is formed primarily during joining. Moreover, several researchers attempted to predict the

✉ Seong Min Hong
hong.sm.jwri@osaka-u.ac.jp

✉ Shinichi Tashiro
tashiro.shinichi.jwri@osaka-u.ac.jp

[1] Joining and Welding Research Institute, The University of Osaka, Osaka, Japan

[2] Department of Welding and Joining Science Engineering, Chosun University, Gwangju, South Korea

[3] Institute for Materials Research, Tohoku University, Sendai, Japan

Published online: 27 January 2026

growth of IMC layer as a function of temperature variation per the unit time which follows the parabolic law of diffusion [11–13]. For the effect of supplementary elements on the formation of IMC, Dong et al. [4] and Su et al. [9] investigated the effect of additional element in the filler wire, and found that Si contained wire can suppress the diffusion of Fe to Al by resulting the Si to permeate to the diffusion path of Fe to Al. Das et al. [11] and Goecke et al. [12] adopted a cold arc GMAW system and changed pulse parameters to join the AA5052 aluminum alloy to hot-dip galvanized (GI) steel. The authors confirmed that the decreased IMC layer thickness with increased joint strength by lowering the heat input by pulsed current. Further, Gatzen et al. [13] reported the Zn coating can increase the arc size or the wet length of aluminum during the cold metal transfer method adopted pulsed GMAW process. Hong et al. [14] simulated the heat loss at the joint interface by zinc evaporation and reported that the mass evaporation of zinc during joining can significantly affect to the formation of IMC layer. Windmann et al. [15] adopted Al-Si3-Mn filler wire with heat input ranges from 240 to 300 J/mm. The authors reported that the maximum joint strength was achieved as 175 MPa with 2–7 μm thick IMC layer. Sierra et al. [16] have used the heat inputs of 120–150 J/mm by pulsed GMAW can form 2 μm thick IMC layer in joining 6XXX aluminum alloy to GI steel with the maximum strength as 180 MPa. Likewise, many of researches indicated that the point of achieving adequate strength of the joint is directly related to the control of lower heat input which in turn the control of IMC layer thickness, but the heat input control to lower level in GMAW process is still challenging and joining parameters for the proper amount of heat input to the joint interface are still ambiguous.

As an effort to control the heat input, several researchers added magnetic field, which is based on the Flaming's law as in Fig. 1, near to the torch to apply the additional Lorentz force into GMAW heat source by varying the field type as cusp, axial, longitudinal or transverse, or rotating shape, respectively [17–24]. The studies found that the application of additional magnetic field can change the arc phenomenon, metallurgical effect or the temperature distribution of the weld pool surface significantly. They showed that the application of additional Lorentz force can lead the suppression of natural convection and the homogenized temperature gradient of the weld pool surface, droplet transfer mode [25–28]. This indicates that the temperature of joint interface during joining can be differed by the electromagnetically manipulated heat and the mass transfer process. However, most of the studies on the application of an additional magnetic field have focused on configurations in which the field is applied near the torch, and have been conducted mainly for bead-on-plate (BOP) welding or homogeneous-metal joints.

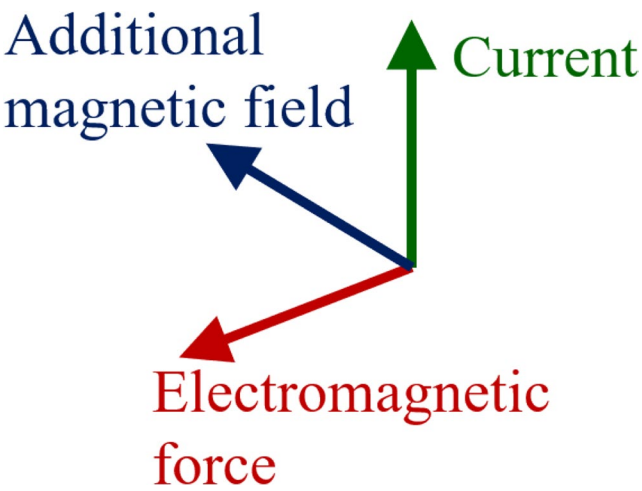

Fig. 1 Electromagnetic field and force

Because the arc is highly sensitive to changes in the applied magnetic field, even small variations in field strength or orientation can lead to noticeable changes in the arc root position and the resulting heat-input distribution, however, careful tuning of the heat source conditions is required in such around-torch configurations. For dissimilar Al–steel thin-sheet lap joints, where localized control of weld-pool flow and interfacial reactions is particularly important [13, 14], an underneath magnetic field applied from beneath the base metal can therefore be considered a useful complementary configuration; however, only a few experimental or quantitative studies have investigated this approach in pulsed GMAW of aluminum alloys to steel, and the corresponding joining mechanisms remain unclear. In the underneath configuration adopted in this study, the magnetic field is suggested through the setting magnetic coils under the Al–GI steel lap joint as a basic study to examine and to reduce direct disturbance of the arc column while enhancing the Lorentz force acting on the molten metal near the joint interface, thereby enabling more selective control of weld-pool flow, wetting behaviour, and Fe–Al intermetallic layer formation in the actual joining region.

Therefore, the purpose of this study is to clarify the joining mechanism and to assess the applicability of an additional underneath magnetic field in pulsed GMAW of aluminum alloy to galvanized steel lap joints. In this approach, electromagnetic coils are placed under the base metals so that the resulting Lorentz force is strengthened in the weld-pool region rather than in the arc column, enabling more direct control of heat and mass transfer at the joint interface. Under the applied underneath magnetic field, an additional Lorentz force is expected to be generated perpendicular to the current flow direction and is expected to accelerate or decelerate the conventionally induced electromagnetic force around the joint area, depending on the field direction.

1.2 mm thick AA5052 aluminum alloy and hot-dip galvanized (GI) steel were adopted as base metals and joined via direct-current (DC) pulsed GMAW to investigate the effect of the additional magnetic-field direction on the joining mechanism and weldability of the aluminum–steel joints. Based on the previous study [29], the welding parameters including the current waveform were fixed, while the direction of a constant additional magnetic field was treated as a process parameter and varied toward the aluminum side, steel side, rear side, and front side, respectively. To elucidate the joining mechanism, arc phenomena including metal transfer and weld-pool surface flow were observed, and the corresponding bead geometry and Fe–Al intermetallic compound (IMC) formation were characterized metallurgically. Finally, the mechanical properties of the joints and their fracture surfaces were evaluated.

2 Experimental method

2.1 Experimental setup

A 12 μm thick Zn layer existing hot-dip galvanized (GI) steel plate and AA5052 aluminum alloy plate were adopted as base metals and joined in a lap configuration using pulsed GMAW with a 1.2 mm diameter AA4047 (Al-Si 12%) filler wire. The dimension of both base metals was 100 (width) × 200 (length) × 1.2 (thickness) mm, respectively. The chemical composition and mechanical properties of the base metals and filler wire are listed in Tables 1 and 2, respectively.

Figure 2 shows the overall experimental setup. As shown in Fig. 2 (a), electromagnetic coils were set between the moving stage and base metals to maintain the position to the welding torch. A schematic illustration of welding set-up is plotted in Fig. 2 (b). The aluminum plate was overlapped by 10 mm on the steel plate, and the joining line was located 2 mm away from the overlapped aluminum edge to the aluminum side with 15° tilting in both the travel angle (15°) and work angle (15°), respectively, to maintain a stable arc. Pure argon gas (99.9%) was employed as the shielding gas, and its flow rate was fixed at 18 l/min. Based on a preliminary study showing one drop per pulse (ODPP) conditions with a 50 Hz of current waveform frequency, contact tip to work distance (CTWD), the average welding current with corresponding wire feed rate, and voltage were fixed as 15 mm, 50 A, 3.7 m/min, 19.6 V, respectively. Furthermore, welding speed was adopted 10 mm/s.

Table 2 Mechanical properties of the base metals and filler wire

Material	Yield Strength (MPa)	Ultimate Tensile Strength (Mpa)	Elongation (%)
AA5052	193	220	12
AA4047	131	268	17
GI steel	164	294	53

A schematic set-up of electromagnetic coils which are for generating additional underneath magnetic fields is plotted in Fig. 2 (c). Two electromagnetic coils were set 10 mm away from the bottom side of the steel base metal, and the coils were connected to the power source with the serial circuit. The electromagnetic coils were fixed at the supporting leg-bar which is set independently from the moving stage to maintain the distance to the joining line. The synthetic vector of magnetic was set al.ong or perpendicular to the joining line to vary the additional magnetic field direction from the steel side to the aluminum side (hereafter, BAL), the aluminum side to the steel side (hereafter, BST), along the joining direction (hereafter, BFR), and the opposite to the joining direction (hereafter, BRE), respectively. Since arc has very high temperature approximately 6500 to 10,000 K [30, 31] and strong radiation, the stable existence of magnetic field at the center of heat source on the joining line was focused in this study, and the electromagnetic flux density distribution before joining was measured to examine the effect of interaction between additional underneath magnetic field and joining process. Corresponding to the setup of the additional magnetic field in Fig. 2, the magnetic flux density environment measured by Gaussmeter is plotted in Fig. 3. The underneath magnetic field was generated using a pair of identical electromagnet coils which was turned by 0.3 mm^2 copper cable for 0.17 A of excitation current following JIS Z 8000-1 standard placed beneath the GI steel sheet with a lift-off distance of 10 mm (Fig. 2). The two coils were connected in series and powered by a DC supply (24 V) to produce a nominal magnetic flux density of 1.0 mT at the top surface of the base metal. The magnetic flux density was measured using

Table 1 Chemical composition and mechanical properties of the base metals and filler wire

Material	Chemical Composition (wt%)								
AA5052	Mg	Mn	Zn	Fe	Si	Cr	Cu	Ti	Al
	2.5	0.1	0.1	0.4	0.25	0.15	0.1	0.15	Bal.
AA4047	Si	Fe	Cu	Mn	Mg	Zn	Be	Al	-
	11.0–13.0	0.8	0.3	0.15	0.1	0.2	0.0003	Bal.	-
GI steel	C	Si	Mn	P	S	Sol-Al	Fe	-	-
	0.012	0.01	0.15	0.015	0.007	0.032	Bal.	-	-

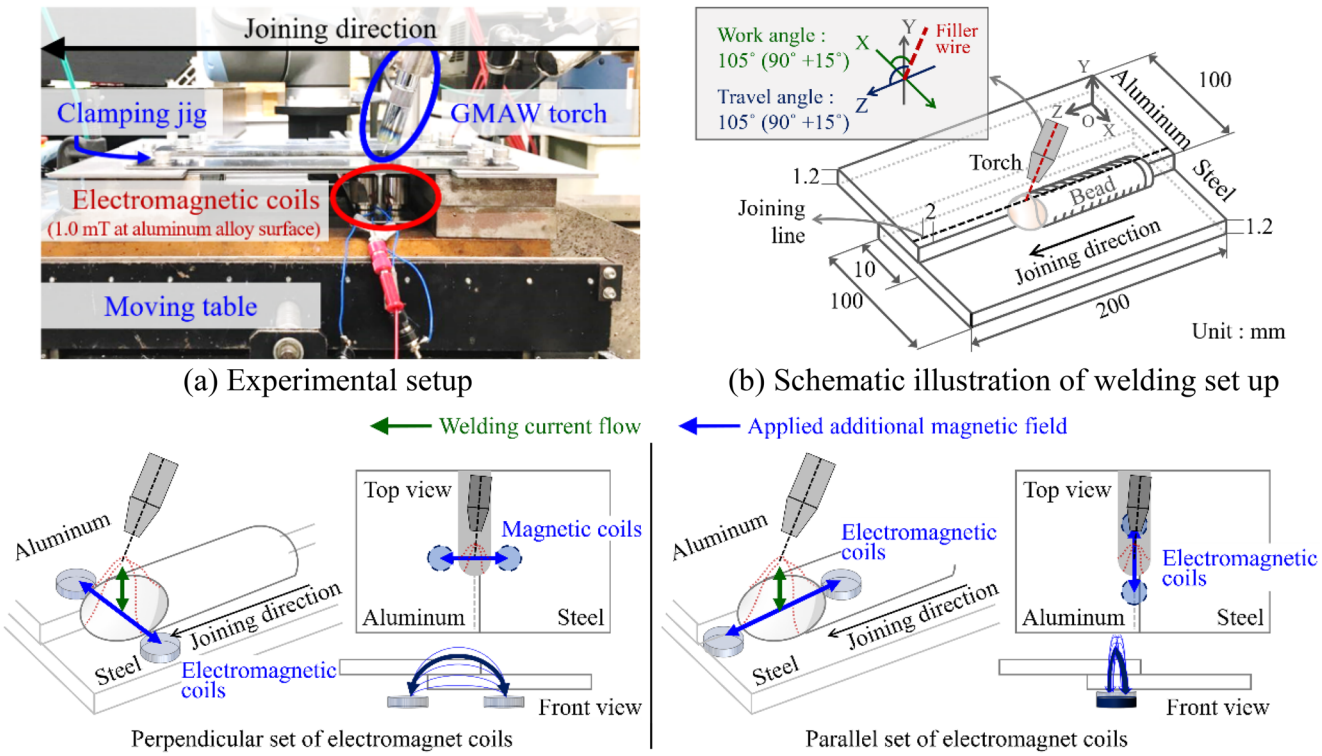

Fig. 2 Experimental set up of additional underneath magnetic field applied pulsed GMAW

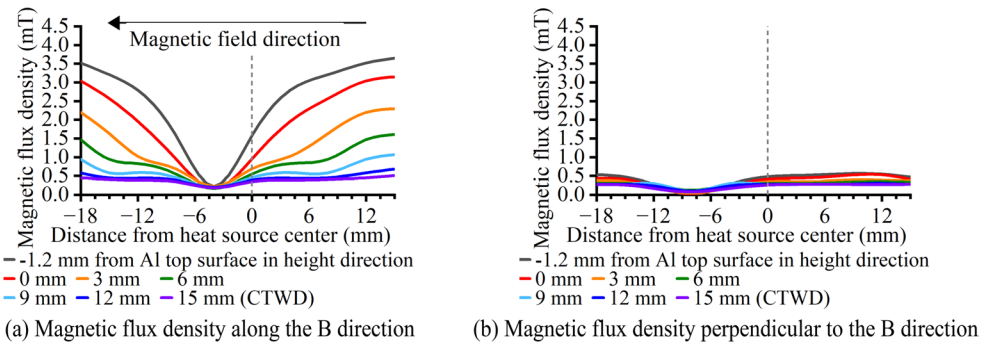

Fig. 3 Magnetic flux density distribution depending on distance from the joining line at different heights. (**a**) Magnetic flux density along the B direction, (**b**) Magnetic flux density perpendicular to the B direction

a Gaussmeter (MG-3003SD Tesla/Gaussmeter, FUSO). For the height-dependent distribution map (Fig. 3), the probe was scanned at $\Delta x = 2$ mm and $\Delta y = 2$ mm intervals perpendicular to and along the joining line direction, respectively, and at $\Delta h = 1.2$ mm and 3 mm intervals in the height direction between the base metal and the torch. At each point, the reading was recorded after stabilization, and three repeated measurements were conducted to assess repeatability. The instrument resolution was 0.01 mT and the repeatability was within ± 0.02 (standard deviation) mT, which was adopted as the measurement uncertainty. Because the coil set was rotated to vary the field direction while keeping the same current and lift-off distance, the field magnitude distribution was essentially identical among orientations and only the field direction relative to the welding coordinates was changed. The welding parameters and applied magnetic field directions in this study are illustrated in Table 3, respectively.

2.2 Experimental method

2.2.1 Arc phenomenon and weld pool flow

The arc phenomenon and corresponding convective pattern of weld pool surface flow were observed to investigate the effect of the direction of underneath additional magnetic field on heat energy distribution to material flow.

In the set-up of arc phenomenon observation, a high-speed camera (Memrecam Q1v, nac Image Technology) was

Table 3 Welding condition and additional underneath magnetic field condition

Current waveform type	Polarity	Current (A)	Wire feed rate (m/min)	Voltage (V)	Joining speed (mm/s)	CTWD (mm)	Shielding gas flow (L/min)	Torch inclination (Working-Travel)	Torch position (mm)
DC pulse	EP	50	3.7	19.6	10	15	18	15 °- 15°	2 to Al
Pulse set	Peak current (A): 265, Base current (A): 25, Peak-Base current time ratio (%): 10, Frequency (Hz): 50								
Condition name by magnetic field	Additional magnetic field (B) direction				Magnetic flux density (mT)		Expected Lorentz force direction		
	From	To							
BXX	Not applied (Conventional)				1.0 at the top surface of Al		-		
BAL	Steel	Aluminum					To rear		
BST	Aluminum	Steel					To front		
BFR	Rear	Front					To aluminum		
BRE	Front	Rear					To steel		

synchronized with a wave data logger (NR-500/NR-HV04, Keyence) which is connected to clamp-meter (3285, Hioki) and workpiece for measuring current and voltage wave form. In here, a function generator (WF1973, NF Corporation) was additionally adopted to send 5 V signal to the camera and data logger simultaneously for triggering. Because the arc plasma in pulse GMA process emits strong radiation and the emission is differed depending on the current wave form, the arc was illuminated by using the varied three neutral-density (ND) filters; (1) ND8 – ND8 – ND8 for the peak current section, and (2) ND8 – ND8 – ND2 for the base current section. A lens (Micro-NIKKOR, Nikon) with 1/4 focus ratio applied 200 mm focal length was adopted, 4000 fps frame rate with 20 μs exposure time was applied to capture the arc in 640 × 480 pixels. In order to observe the arc phenomenon clearly, the entire arc was observed from two angles: (1) viewing angle for the arc front that is observed from the welding finish location to the start location direction and (2) viewing angle for the arc side from the steel side perpendicular to the joining line.

In case of the convective patterns of weld pool surface, the flow pattern was observed by tracing the movement of 0.03 mm diameter zirconia particles through the 640 nm wavelength laser assisted 4000 fps high-speed video camera (Memrecam Q1v, nac Image Technology) system synchronized with data logger. In this system, an additional lens (AF Micro Nikkor 200 mm, Nikon) was attached with a bandpass filter (THORLABS UV/IR cut filter MP-49 S) to the high speed camera system interacting with a laser light source which provides a strong monochromatic light to irradiate the strong radiation of arc plasma covering the weld pool surface area. As shown in Fig. 4 which shows the results of spectral analysis of Ar arc plasma in previous study [29], the emission line spectrum of the Ar arc has high radiant intensity in the region of 690 to 850 nm. In contrast, the radiant intensity around 640 nm shows lower than the region of 690 to 850 nm. This indicates that the use of

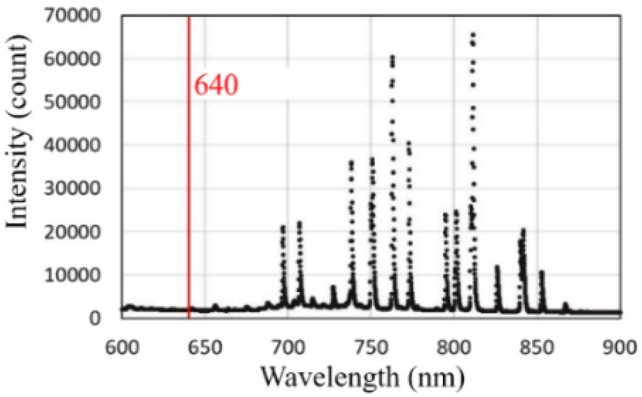

Fig. 4 Line profile of argon arc spectrum [34]

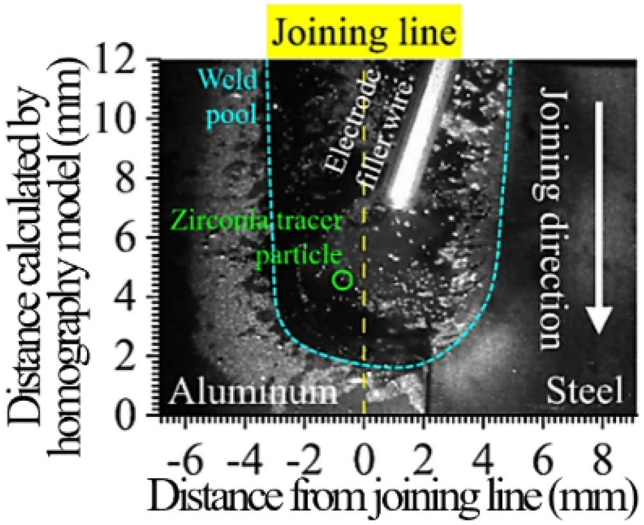

Fig. 5 Defined coordinate of weld pool flow observation

640 nm laser light source and corresponding bandpass filter allows to observe the molten pool with reflected light while suppressing the influence of arc light. To capture the weld pool images by removing the wavelength of arc plasma as shown in Fig. 5, the laser light source was synchronized with the high-speed camera to irradiate only during the camera exposure time. 6.4 µs laser pulse width was exposed in every 10 µs with 4000 fps of high-speed camera recording in 640 × 480 pixels. After the observation of zirconia movement, the coordinate was calculated through homography model [32, 33] from the captured image through the camera. Defining the X coordinate as perpendicular to the joining line and Y coordinate as opposite direction to the joining direction, respectively, the location of particle followed the assumption that X = 0 mm is on the meeting point of X coordinate and joining line. The tracing of zirconia particle trajectories and the calculation of their velocities were conducted so as to minimize the influence of the characteristic changes in the peak- and base-current segments and the pool-surface fluctuation induced by droplet impingement. First, for each tracer, the frame in which a zirconia particle first emerged at the weld-pool surface was defined as the initial tracing time, and its position in the subsequent frames was tracked continuously. By comparing these images with the current waveform recorded by the synchronized data logger, the end of the pulse cycle immediately before the onset of the next peak-current segment was defined as the second reference time, and the instantaneous velocity was calculated from the change in zirconia particle coordinates between these two times divided by the corresponding time interval. Thereafter, this second reference time was updated pulse by pulse, and the same procedure was repeated until the zirconia particle was observed to cease its motion in the X-direction due to pool solidification and to move along the Y-direction at a speed equal to the nominal joining speed. By using only this relatively stable time window within each pulse cycle, frames in which the tracer image could be disturbed by droplet impingement or rapid arc fluctuations were excluded, thereby minimizing the frame-to-frame tracing error.

The overall observation setup for the arc phenomenon and convective patterns of weld pool surface is schematically illustrated in Fig. 6.

2.2.2 Metallurgical and mechanical evaluation

Cross-sectional views of the joint samples were etched with 5% nital reagent for 5 s and modified Tucker's reagent for 10 s after polishing with SiC papers of 400 to 4000 grit and 9, 3, and 1 µm diamond suspensions, and an SEM–EDS analysis was conducted to determine and characterize the IMC layer at the joint interface. SEM-EDS analysis were conducted to investigate the formation of Fe-Al IMC at the joints interface and to characterize their element

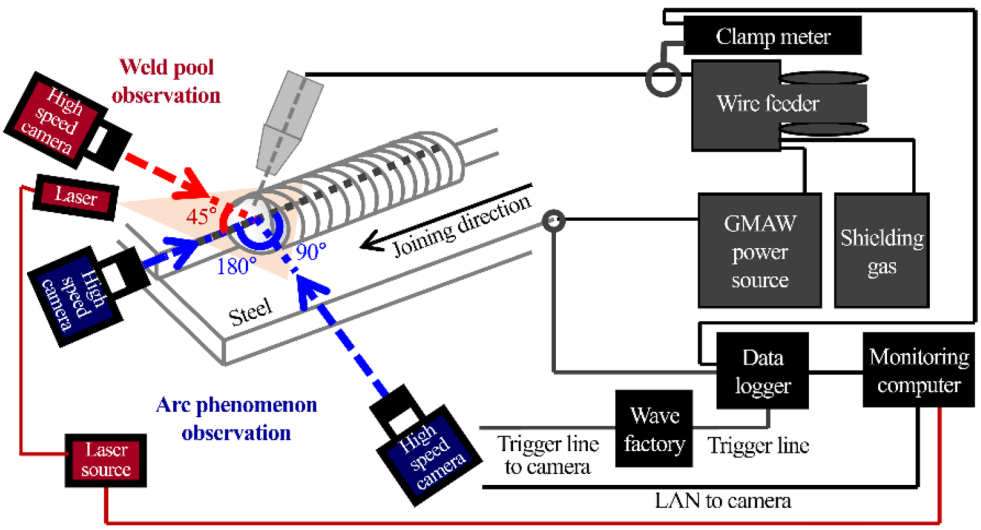

Fig. 6 A schematic illustration of arc phenomenon and convective weld pool surface flow observation setup

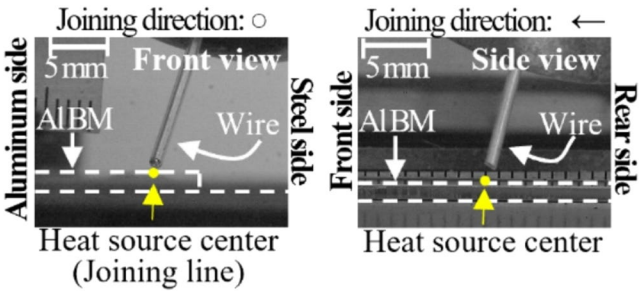

Fig. 7 Location of arc phenomenon observation; front view and side view

composition. Moreover, the tensile-shear test based on ASTM E8 standard was carried out on seven specimens for each process condition to investigate joint strength through the Instron-type tensile-shear strength testing machine at a crosshead speed of 1 mm/min, and the fracture surface of the samples were compared by SEM analysis.

3 Result and consideration

3.1 Arc phenomenon

Based on Fig. 7 which illustrates two different observation positions (Front and side view) and corresponding scale, the arc shape and corresponding location of the arc formed on the base metal was observed to investigate the effect of the direction of underneath additional magnetic field on the heat source formation. Furthermore, corresponding pulsed current – voltage wave forms during 160 ms after when the welding heat source is reached to approximately 100 mm away from the welding start location is measured. The measured welding current-voltage wave forms are plotted in Fig. 8 (a), and the magnified waveforms from 98 ms to 121 ms which showed the overlapped pulse cycle are shown in Fig. 8 (b).

Although the welding process parameter was fixed, the actual pulse frequency was increased slightly as B was applied. Compared to the average frequency of current – voltage waveforms in BXX in Fig. 8 (a); 51 Hz, slightly higher but different frequencies were achieved as the B direction was changed (52 Hz by BAL, 53 Hz by BST, 55 Hz by BFR, and 54 Hz by BRE) indicating the decreased heat input to the base metal and increased numbers of droplet. Considering one of the driving forces that decides the droplet detachment is Lorentz force as schematically shown in Fig. 9, it can be explained that the addition of external underneath magnetic field increased the Lorentz force between the molten wire and the edge of the solid wire as simply described in Eq. (1) to Eq. (2), so that the pinch effect is slightly accelerated and the numbers of droplet detachment is increased.

$$F = J \times B_{conv.} \tag{1}$$

$$F = J \times (B_{conv.} + B) \tag{2}$$

At here, $\boldsymbol{F}$ is Lorentz force acting on a point particle with electric charge which flows with current density $\boldsymbol{J}$. $\boldsymbol{B_{conv.}}$

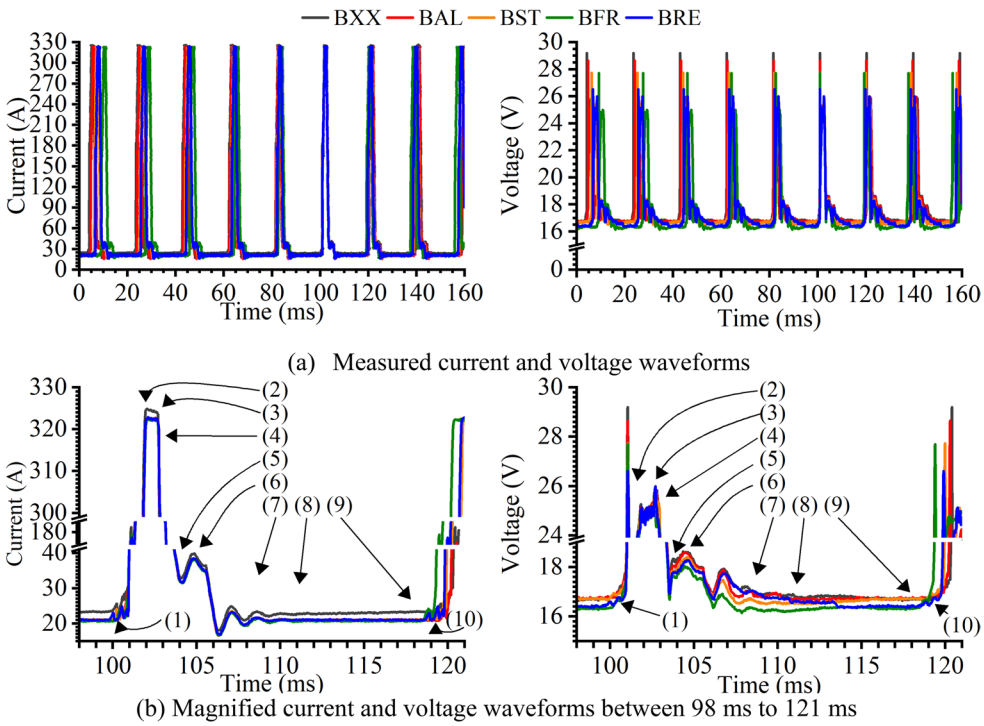

Fig. 8 Direction of additional underneath magnetic field varied voltage and current waveforms. (**a**) Measured current and voltage waveforms (**b**) Magnified current and voltage waveforms between 98 ms to 121 ms

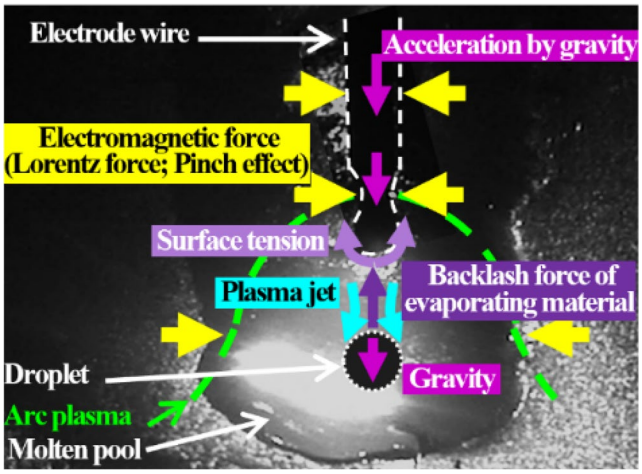

Fig. 9 Schematic illustration of forces and their directions in metal transfer during GMAW

Indicates magnetic field density during welding, and ***B*** is a density of additional underneath magnetic field, respectively. Furthermore in Fig. 8 (b), both the current and voltage were decreased as B applied, and the achieved current – voltage values were similar. Especially in Fig. 8 (b) (2) to (3), although the voltage waveforms of B applied conditions during the peak current session were similar with BXX, the average peak current until the droplet detachment in B applied conditions (320.4 A in BAL, 320.3 A in BST, 320.1 A in BFR, and 320.3 A in BRE) were lower than that in BXX (325.3 A) indicating the required power (***P=VI***; ***V*** is voltage, ***I*** is current, respectively) which is to detach the molten wire against to the surface tension force from the molten wire. Similarly, during the base current session as shown in Fig. 8. (4) to (10), overall current and voltage of B applied conditions (23.4 A in BAL, 23.6 A in BST, 23.7 A in BFR, and 23.6 A in BRE) were slightly lower or lower than BXX (26.3 A). Interestingly, however, the voltage in BFR was gradually increased from 16.2 V to 16.7 V in Fig. 8. (7) to (9), but that in BRE was decreased gradually from 17.6 V which is the similar value of BXX (17.8 V) to lower value as 16.4 V. Since the voltage is highly related with arc shape and length which is related to the resistance and is easily affected by Lorentz force, this will be discussed later together with arc shape images. From slightly increased frequency and lowered current and voltage waveforms of B applied conditions, however, it can be concluded that the existence of additional external magnetic field during the welding can affect to the bead formation and actual input heat to the base metal.

High-speed video images of arc phenomenon observed from the opposite to the joining direction are shown in Fig. 10 as the front view, and that observed from the steel side are shown in Fig. 11 as the side view, respectively. The plotted arc images in Figs. 10 and 11 are corresponded to the variation of the current – voltage in a pulse cycle which are marked as (1) to (10) in Fig. 8 (b). In case of (1) in Figs. 10 and 11, it shows the end of the previous pulse cycle which is in the base current section which is in same timing of the pulse cycle with (10). (2) to (3) are the arc during the peak current section and following (5) to (10) are that during the base current section, respectively. Hence in here, comparison of arc phenomenon will be mainly focused on (1) to (9). In addition, due to the arc during the peak current section has much strong radiation than during the base current section has, arc in the peak current during (2) and (3) were taken by using a combination of three ND 8 filters but the rest of period were taken by that of two ND 8 filters and a ND 2 filter.

Figure 10 (a) describes the front view of arc phenomenon in a current waveform cycle of BXX. The arc showed a slightly asymmetric shape that the arc at the aluminum side with longer radius compared to the arc at the steel side, and the front side of the arc formed the longer radius than the rear side in the side view as shown in Fig. 11 (a). Since the strong electric arc tends to maintain its shape with strong radiation as brighter emission, the tilting of the torch leads the formation of shorter radius of arc to the tilted side and vice versa on the base metal. Moreover, because the heat energy of arc follows Gaussian heat energy distribution, it was able to notice that the asymmetric ellipsoidal shape was distributed as lower energy heat density in wider range to aluminum side as relatively darker arc images. From this, the drastic heating of aluminum base metal was prevented, compared to the heat energy distribution to the steel side. In comparison of (9) to (10) in both Fig. 10 (a) and Fig. 11 (a), the increase of light intensity of the arc in grey scale value was observed in (10) as more bright color in the arc during the increase of current which follows the increase of voltage as shown in Fig. 8 (b). This indicates the start of new current wave form which can be confirmed as the same as (1) to (2). It was also observed that that the current was soared from (1) to (2) in Fig. 8. (b) as to approximately 325 A, and the current was maintained to (3) until the molten filler wire is detached as shown in (4). Especially during (2) to (3), the Lorentz force which is proportional to the square current detached the molten from solid electrode filler wire before the diameter of the molten wire is growing bigger than that of the solid wire. It indicates that the globular metal transfer as one ODPP. In the side view of BXX in Fig. 11 (a), cathode spots were formed on both base metal and on the weld pool, respectively, as shown as the bright and high intensity spots due to its high current density. Especially in (1), and (5) to (9), slight movement of arc root along the locations where the cathode spots were formed. This is attributed to the lower work function value of the aluminum oxide permits formation of the arc root as listed in Table 4 which

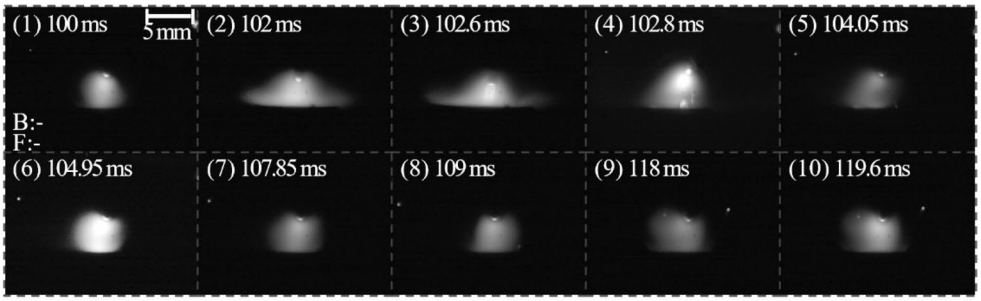

(a) Front view of arc phenomenon in BXX

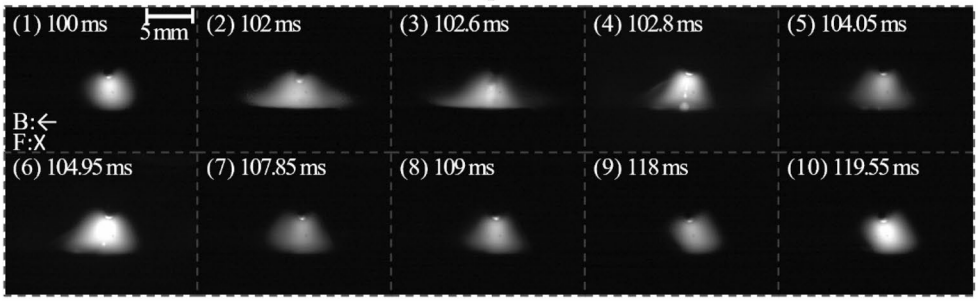

(b) Front view of arc phenomenon in BAL

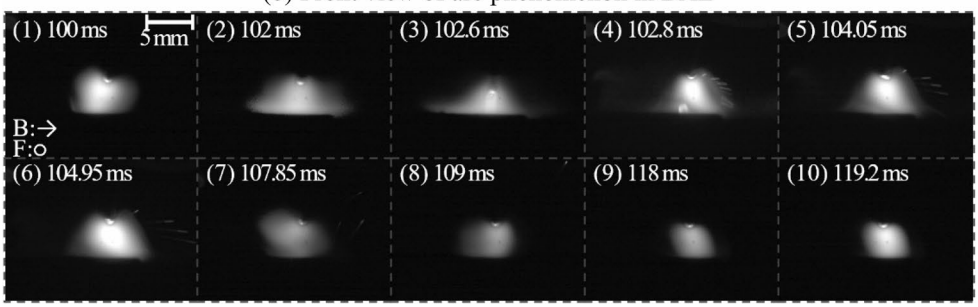

© Front view of arc phenomenon in BST

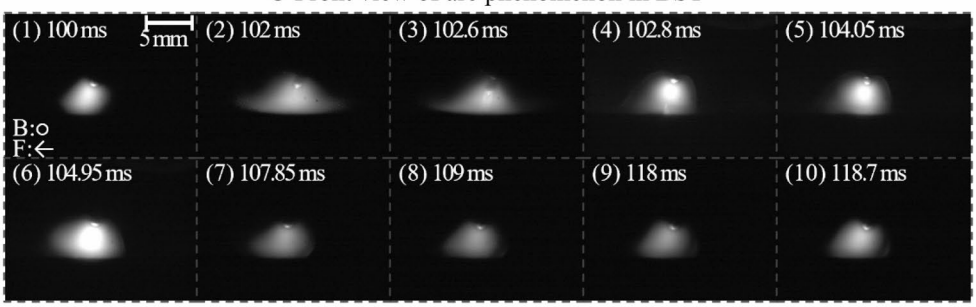

(d) Front view of arc phenomenon in BFR

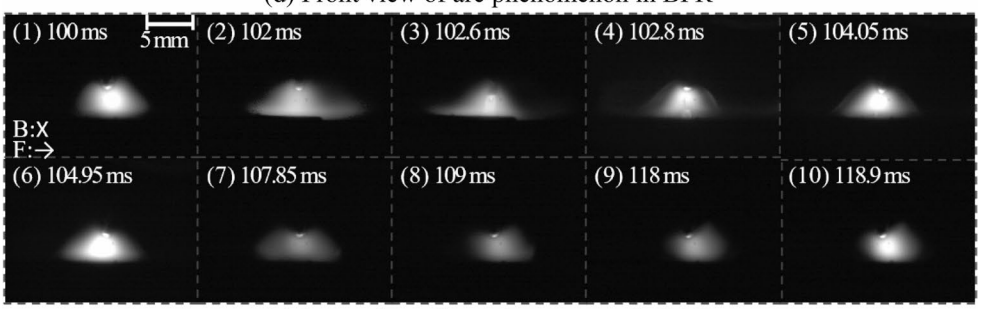

(e) Front view of arc phenomenon in BRE

Fig. 10 Arc shapes during a pulsed wave form; observed from the opposite to the joining direction. (**a**) Front view of arc phenomenon in BXX, Front view of arc phenomenon in BST) (**b**) Front view of arc phenomenon in BAL, (**c**) Front view of arc phenomenon in BST (**d**) Front view of arc phenomenon in BFR, (**e**) Front view of arc phenomenon in BRE

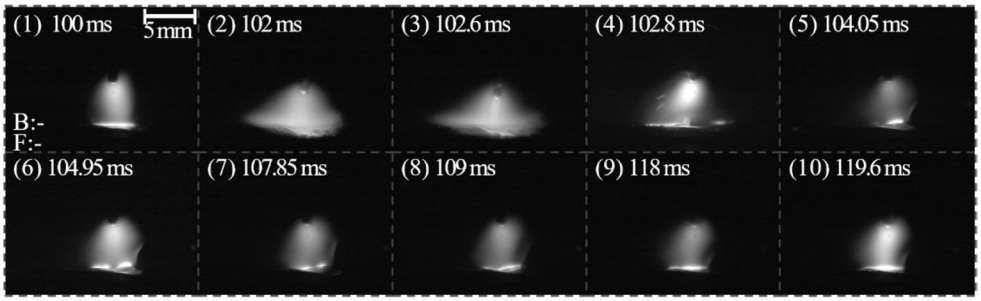

(a) Side view of arc phenomenon in BXX

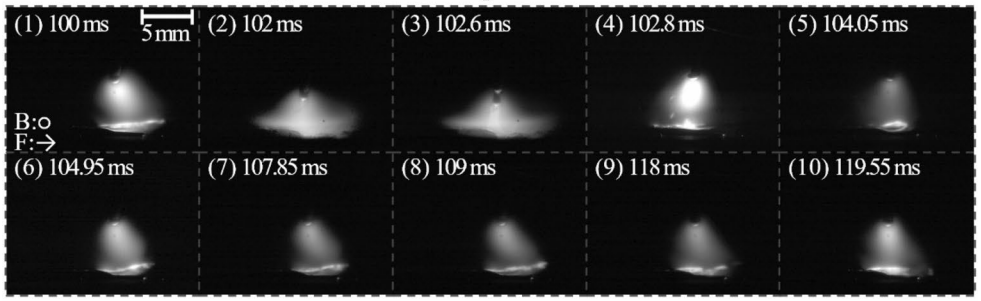

(b) Side view of arc phenomenon in BAL

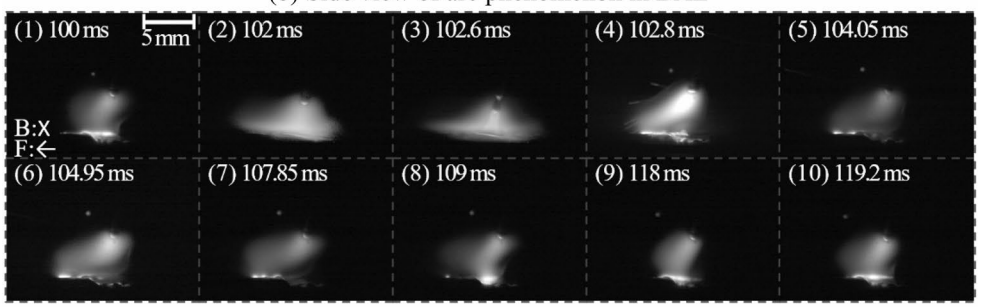

(c) Side view of arc phenomenon in BST

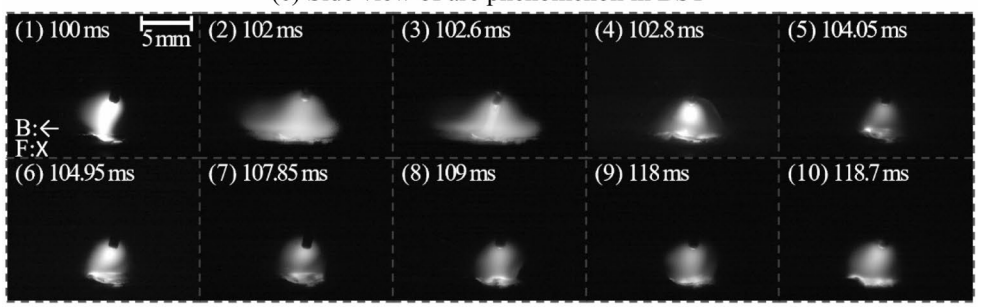

(d) Side view of arc phenomenon in BFR

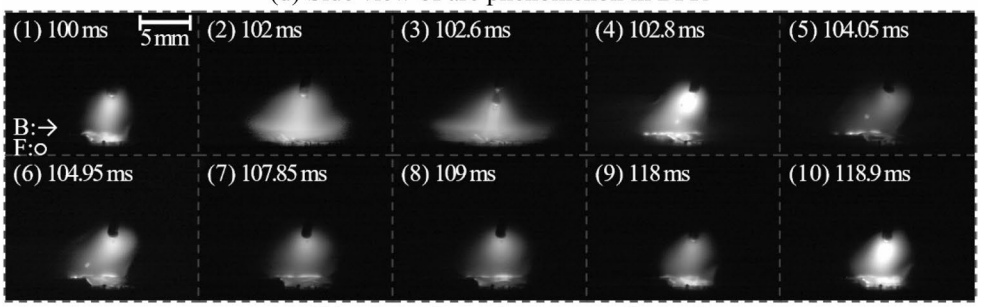

(e) Side view of arc phenomenon in BRE

Fig. 11 Arc shapes during a pulsed wave form; observed from the steel side. (**a**) Side view of arc phenomenon in BXX, (**b**) Side view of arc phenomenon in BAL, (**c**) Side view of arc phenomenon in BST, (**d**) Side view of arc phenomenon in BFR, (**e**) Side view of arc phenomenon in BRE

Table 4 Material properties of al, al oxide, Fe, Zn, and Si [29]

Properties	Al	Al_2O_3	Fe	Zn	Si
Melting temperature (K)	933	2345	1808	693	1683
Boiling temperature (K)	2792	-	3134	1180	3538
Work function (eV)	4.26	3.36–3.84	4.81	4.4	4.85
Ionization voltage (V)	5.99	-	7.87	8.15	9.39

provides an example of material properties of a possible aluminum oxide (Al_2O_3) on the aluminum base metal. Since the cathode spot is known that its high current density provides intensive joule heating at its formation area, it indicates that the aluminum oxide was removed by the cathode spots on the base metal surface before and during the melting of the aluminum base metal. On the other hand, this high heat energy at the base metal surface can indicate that there is possible formation of an excessive Fe-Al IMC layer, porosities due to the low boiling point of Zn, and deformation by the high thermal expansion coefficient of Al and Zn. About the arc phenomenon when the **B** was applied as shown in (b) to © in Figs. 8, 10 and 11, respectively, it showed similar tendency with BXX that the current was elevated quickly and maintained the strengthened arc with wire melting in the peak current section. Then, the current was decreased drastically with the detachment of the molten wire as globular type metal transfer in (3) to (4) by showing ODPP.

Since the arc plasma during electrode positive polarity DC pulsed GMAW in this study is a flow of electron from the base metal surface to the filler wire and characterizing the arc formation only as the Gaussian distribution is ambiguous to define, the overall shape was simply described but the tilting or expansion of arc was characterized by the range of arc formation on the aluminum base metal which is detected by grey scale value as intensity. The arc cover range in representative timings when in peak current (2), base current (8), and near to the end of base current Sect. (9) are compared in Fig. 12.

Although the B applied conditions followed similar metal transfer with BXX, it was observed that the arc was bended in different directions; the arc was tilted to the rear side, front side, the aluminum side, and steel side in BAL, BST, BFR, and BRE, respectively.

In case of BAL, the comparison of arc dimension on the aluminum base metal in Fig. 12 (a) to (c) did not show the clear change from BXX. However, the arc observed from side view in Fig. 11 (b) showed the arc was expanded or tilted significantly to the rear side which is along the

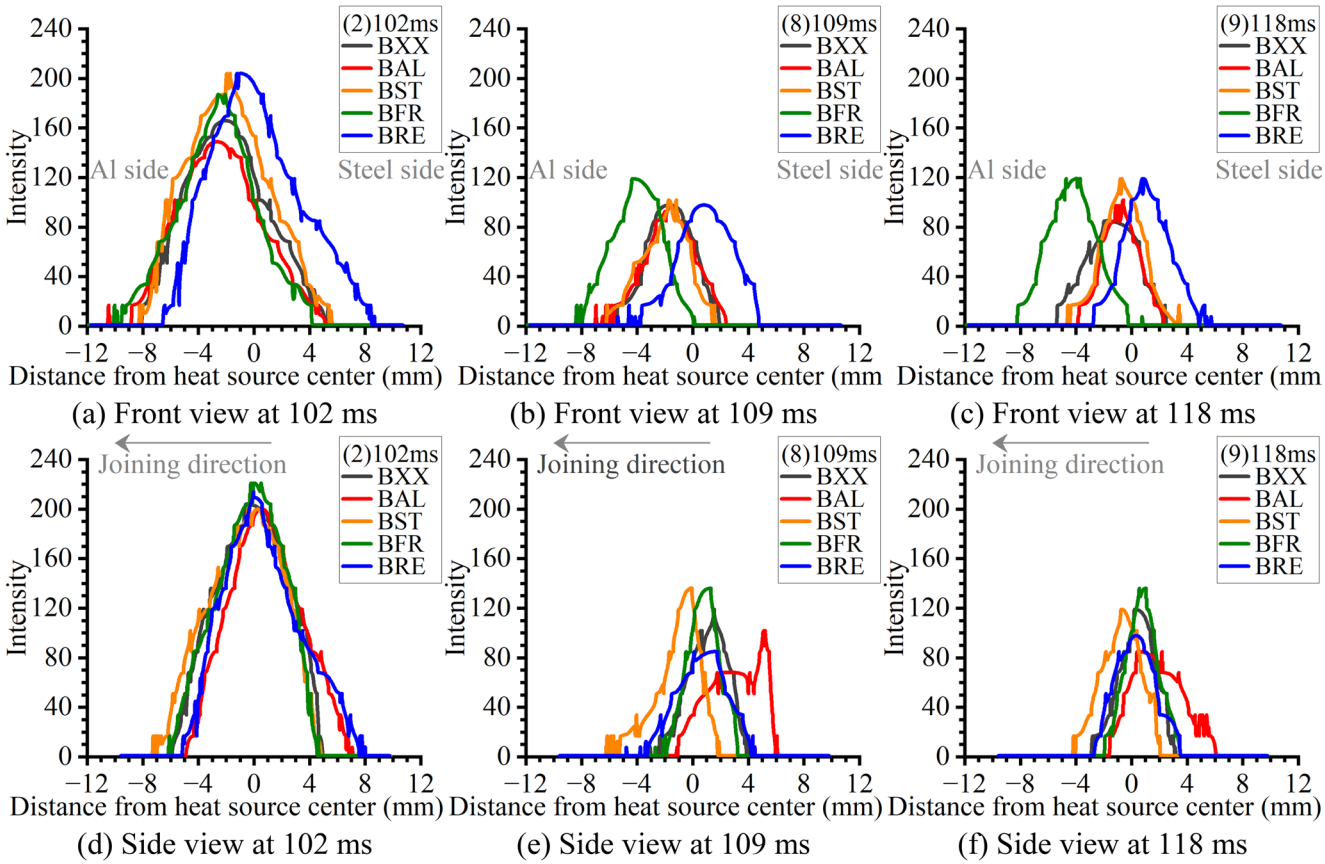

Fig. 12 Arc plasma location on the aluminum surface with its intensity depending on the time. (**a**) Front view at 102 ms, (**b**) Front view at 109 ms, (**c**) Front view at 118 ms, (**d**) Side view at 102 ms, (**e**) Side view at 109 ms, (**f**) Side view at 118 ms

direction of additionally added Lorentz force in both peak and base current section. Compared to the side view of arc shape by BXX in Fig. 11 (a), BAL showed that the rear part of the arc formed thicker and smooth shape than the rear part of arc in BXX. In contrast, the front part of the arc in BAL showed relatively flatter bottom edge side with narrower center width than the arc in BXX. Especially in Fig. 12 (d) which is at the peak current section, the arc of BAL was formed in shorter range as approximately *5 mm* to front side than that of BXX as 6 mm, but the rear side showed that the arc by BAL was formed to *7 mm* which is longer than that by BXX as 5 mm. In total arc range in the peak current, BXX formed as approximately 11 mm but BAL formed slightly increased 12 mm. During the base current section in Fig. 12 © and (f)which show much lower current as in Fig. 8 (b), the arc cover range showed much clear gap. In this period, arc by BXX was formed approximately from 2.5 mm in the front side to the 3.6 mm in the rear side range as totally 6.1 mm, but BAL formed *1 mm* in the front side with *6 mm* in the rear side as total 7 mm which is also slightly increased range than BXX.

In case of BST in Fig. 11 ©, the arc shape from the side view showed the opposite tendency compared to the BAL showed. Contrary to the shape of arc front in BAL, that in BST showed thicker and smooth shape of arc at the arc front part but the arc rear part showed flatter bottom edge compared to the BXX and BAL. In case of the arc dimension of BST, it was measured as approximately 7.2 mm in arc front side to 5 mm in the rear side during peak current in Fig. 12 (d), and 5.3 mm in arc front side to 2 mm in the rear side during the base current in Fig. 12 © and (f), respectively, and their total range was wider than BXX. In the front view as in Fig. 10 © and Fig. 12 (a) to (c), however, not that much of change was observed which is similar as BAL.

Considering that B generates the additional Lorentz force (hereafter, F) interacting with the welding current, which is from the wire to the base metal, the direction of F during BAL is to be the rear side and that during BST is to be the front side, respectively. This indicates that the newly formed F vector was added to the conventional Lorentz force vector, so the increased force in the area where the conventional and the newly formed force are in the same direction pushes the arc to the opposite area where the force is reduced. Hence from here, it can be concluded that the dimension of arc on the base metal can be decided by the F, and its location is also determined by F direction.

Similar with the arc front and rear part of BAL and BST observed from the side view, the comparison of the arc shape by BFR and BRE confirmed that the front view showed the opposite tendency to each other, and in detail, BFR showed the arc range from 10 mm in the aluminum side to 4.2 mm in the steel side, and BRE showed 6.5 mm in the aluminum side to 8.9 mm in the steel side during the peak current section, respectively, while BXX showed 8 mm in aluminum side to 5.5 mm in steel side. In addition, during the base current section, BFR showed the arc range from 8.4 mm in the aluminum side to 0.1 mm in the steel side, and BRE showed 3.7 mm in the aluminum side to 5.4 mm in the steel side during the base current section, respectively. In the base current section, the arc range of BXX in the front view was from 5.4 mm in the aluminum side to 2.3 mm in the steel side. However, there was almost no change in arc shape at the front and rear part which are observed from the side view as can be compared in Fig. 12.

Therefore, the $\boldsymbol{B}$ deflects the arc via $J \times (B_{conv.} + B)$ on $\boldsymbol{B}$ applied direction and $J \times (B_{conv.} - B)$ on the opposite direction, thereby redistributing the heat-flux onto the aluminum base-metal surface in a direction-dependent manner. Specifically, BAL promotes rear side direction development of the arc, BST forward development, and BFR and BRE lateral spread toward the aluminum and the steel sides, respectively, leading to lowered heat input per unit area by mitigating the energy density to the corresponding regions on the aluminum surface. Because frames during peak and base current used different ND filters, interpretation was carried out through spatial patterns within each stage rather than absolute intensities, noting that the base-current period exhibits a more pronounced spread due to weaker arc inertia or confinement by lenses. Cathode spots contributed concentrated Joule heating and oxide cleaning along their formation/trace paths. While arc momentum/confinement during the peak current limits relatively the magnetic effect, the base-current period shows a broader magnetic-driven lateral spread, widening the heat-supply area to the Aluminum. Since the metal transfer remained globular ODPP for all cases, the primary role of the field is not to change the transfer mode but to reorganize the heat source energy-density map on the Al surface with increased frequency. In sum, by choosing the field orientation as a design variable, one can deliberately bias and enlarge the heat-flux distribution toward the aluminum surface, establishing the initial/boundary conditions for the subsequent weld-pool surface convection while suppressing local overheating and redistributing the shear-driving fields.

3.2 Weld pool surface flow

Based on the defined coordinates in Figs. 5 and 13 (a) to (e) plots the convective pattern of the weld pool surface during the joining, and Fig. 13 (f) plots the location of droplet impingement which affects to the weld pool flow by physical contact of molten wire to the weld pool. Because the physical impingement of droplet fluctuates the weld pool with unstable wave, the origin of coordinate in overall flow

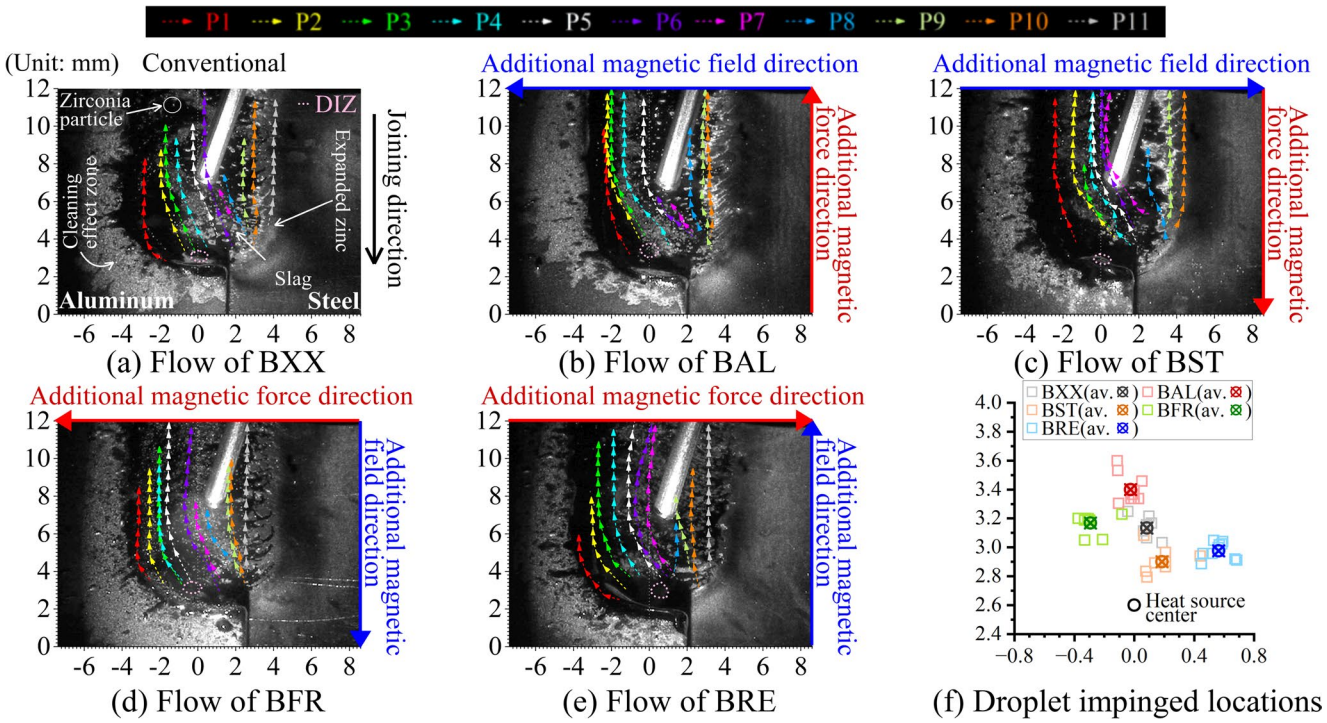

Fig. 13 Comparison of convective weld pool surface flow and droplet impingement. (**a**) Flow of BXX, (**b**) Flow of BAL, (**c**) Flow of BST, (**d**) Flow of BFR, (**e**) Flow of BRE, (**f**) Droplet impinged locations

investigation and that in flow velocity were defined independently in this study. A floated particle near the root (aluminum side) was defined as P1, and the number was increased to P11 as close to the toe (steel side), and the movement of each specific particle was colored differently. The curves in each graph in Fig. 13 represent the moving trajectories of the zirconia particles, and the velocity of each particle is correspondingly illustrated with same colors in Fig. 15. Defining the joining line as the X-coordinate origin in Fig. 13, the moving trajectories of the zirconia particles were obtained by extracting the coordinates of the particles in the images. The movement of tracer particles were obtained in every 0.1 s which is corresponding to five cycles of the current waveform. Correspondingly in Fig. 15, the origin of coordinates was re-defined as the center of the DIZ to simplify and minimize the errors of collected data from the fluctuation of weld pool by the impact of the droplet during the impingement. In Fig. 15 (a) to (e), the X-axis shows the distance between the center of the droplet impinged zone (DIZ) to the tracer particle, and the Y-axis represents the velocity ($| V |$) of the particle. Following the same coordinate system with Fig. 15 (a) to (e), Fig. 15 (f) to (j) describes the X-velocity (V_x) of weld pool which indicates the velocity variation in the perpendicular direction which is from the DIZ to toe side and to the root side. Furthermore, Fig. 15 (k) to (o) shows the backward longitudinal velocity of the tracer particle as Y- velocity (V_y).

In all conditions in Fig. 13, the flow direction of the particles, especially P2 to P8 in BXX, BAL, BST, BFR and P2 to P7 in BRE, respectively, showed two flow pattern stages subsequently: (1) the aluminum side directional backward flow, and then (2) the backward flow.

In the first time, the weld pool surface flow showed the biased surface flow pattern to the aluminum side from the steel side. Notably, it can be also observed that the zinc coating next to the molten aluminum at the toe side is expanded indicating the melting of the zinc layer. After melting of the zinc layer, the detached or split top surface of the steel side layer, which can be considered as slag or zinc oxide firm, was floated along the weld pool surface continuously as backward climbing to the aluminum side. In here, furthermore, the floating of zirconia particles, which were set between the base metals along the joining line, was observed. Most of floated particles in this area moved to the aluminum side firstly by backward climbing of weld pool surface with relatively higher velocity, and then they moved backward with deceleration. Although several studies found temperature gradients of weld pool surface in thin plate welding is not so much drastic [26], the aluminum toward backward climbing flow indicates that the weld pool has inward flow pattern which follows the Marangoni effect 'in' the weld pool. Therefore, as shown in Fig. 14, it can be explained that the zinc evaporates drastically inducing the heat loss at the joint interface through its latent heat, so that

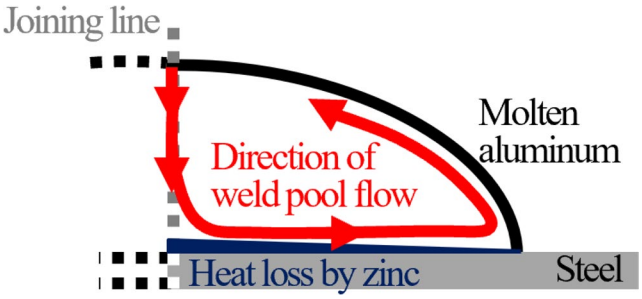

Fig. 14 Schematic illustration of weld pool flow in cross-sectional view

the temperature gradient of the molten aluminum between at the top surface and at the joint interface is being drastic. This points that the surface tension gradient of the molten aluminum is increased, hence it can be inferred that the accelerated Marangoni effect formed the backward climbing tendency on the weld pool surface flow.

Assuming the distance from DIZ center location as s and comparing the velocities curves; $|V|$, V_x, V_y of BXX in Fig. 15 (a), (f), (k), BXX in Fig. 13 (a) shows the tracers curve toward the aluminum side ($x < 0$) and move rearward ($y > 0$) rapidly in near-DIZ ($s = 0 - 2mm$), with $|V|$ and V_y attaining their maxima while $V_x < 0$. In the transition region ($s = 2 - 5mm$), the trajectory curvature decays quickly, $|V|$ and V_y decrease mildly, and V_x crosses zero, neutralizing the lateral bias. After that, in the rear side of weld-pool region ($s = 5 - 9mm$), the flow becomes a quasi-linear rearward drift at low speed, with V_x settling to small positive values. This indicates that, even without ***B***, the combined action of plasma-jet shear and Marangoni shear aligned with the local thermal field around the DIZ drives an initial aluminum-biased rearward flow, which relaxes to a linear, low-speed rearward state as the increase of s.

Under the BAL in Fig. 13 (b), combining with Fig. 15. (b), (g), (l), the tracers curve toward the aluminum side ($x < 0$) and move rearward ($y > 0$) rapidly in the near-DIZ ($s = 0 - 2mm$), with $|V|$ and V_y starting larger than in BXX over the same interval. V_x begins from the toward the aluminum side but crosses zero within a short distance, indicating suppressed lateral spread compared with BXX. In the transition region ($s = 2 - 5mm$), the trajectory curvature decays faster than in BXX; $|V|$ and V_y decrease mildly while V_x stays near zero or small positive values, keeping the lateral component weak. By the rear side of the weld-pool region ($s = 5 - 9mm$), the flow has already settled which is similar to BXX, but reached at a shorter distance. Mechanistically, the applied additional magnetic field supplies a rearward F that adds constructively to the baseline plasma-jet and Marangoni shear driving the backflow. With equal pulse energy, the heat flux over the aluminum surface is more broadly dispersed with reducing heat input per unit length, which may reduce the relative influence of

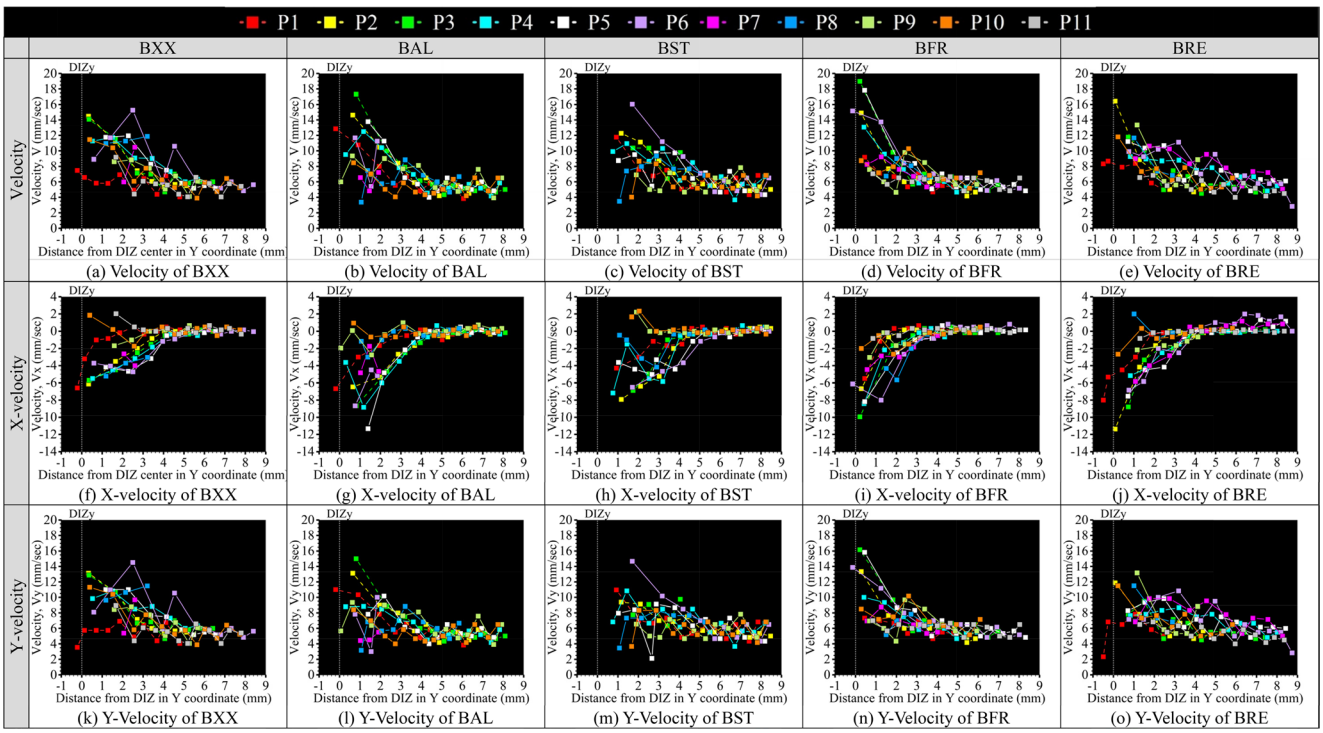

Fig. 15 Comparison of weld pool flow velocity. (**a**) Velocity of BXX, (**b**) Velocity of BAL, (**c**) Velocity of BST, (**d**) Velocity of BFR, (**e**) Velocity of BRE, (**f**) X-velocity of BXX, (**g**) X-velocity of BAL, (**h**) X-velocity of BST, (**i**) X-velocity of BFR, (**j**) X-velocity of BRE, (**k**) Y-Velocity of BXX, (**l**) Y-Velocity of BAL, (**m**) Y-Velocity of BST, (**n**) Y-Velocity of BFR, (**o**) Y-Velocity of BRE

lateral temperature gradients ($\partial T/\partial x$) and accentuates the rearward temperature gradients ($\partial T/\partial y$). Consequently, relative to BXX, BAL consistently exhibits enhanced initial V_y, an earlier zero-crossing of V_x, and a shorter distance to linearization.

In opposite, tracers, which is in the DIZ-normalized coordinate s of BST from Fig. 13. (c), start with smaller $|V|$ in Fig. 15 (c) and V_y in Fig. 15 (h) than BXX and BAL, while V_x in Fig. 15 (m) quickly crosses from negative to positive, yielding pronounced lateral spread; this persists through the transition and the rear side of weld-pool regions, producing a delayed linearization and a broader trajectory bundle. Mechanistically, the field supplies a forward F that partially cancels the baseline rearward driving (plasma-jet and Marangoni shear), reducing V_y. Compared with BAL, which adds rearward driving as larger V_y, earlier V_x to be 0, and shorter distance to linearization, BST consistently shows lower V_y, sustained positive V_x, and a delayed linearization.

Subsequently, BFR in Fig. 13 (d), Fig. 15 (d), (i), (n), shows that the tracers in near-DIZ ($s = 0 - 2mm$) exhibit weak initial curvature toward the aluminum side and limited rearward acceleration, that is smaller starting of $|V|$ and V_y than in BXX and BAL. V_x begins as negative but increases with a shallow slope, leading to a delayed zero-crossing and suppressed lateral spread. In the transition region ($s = 2 - 5mm$), the paths are linearized early into a rearward drift, $|V|$ and V_y stabilize at low levels, and V_x passes near zero slightly but gradually. In the rear side of weld pool region ($s = 5 - 9mm$) a low-speed linear rearward flow persists, with V_x approaching small positive values. In this case, it can be explained that the applied magnetic field produces a F configuration which disfavors the initial climbing by showing effective inducing of a toe-down and root-up tendency in the weld pool as summarized in Fig. 16 which shows an expected ***F*** in the weld pool during welding. Although the F mainly pushes to the alumium side on the weld pool surface, especially in Fig. 16 (c), it is inferred that the expected F in the weld pool accelerates toe-down and root-up tendency in weld pool morphology, hence it limits mechanically the aluminum toward and backward flow. Thereby, the baseline rearward driving is being attenuating. Compared to BXX, BFR shows smaller initial V_y and earlier linearization but at lower overall speeds, together with a later V_x zero-crossing and weaker lateral spread; compared with BAL, which adds rearward driving with larger V_y and earlier V_x to be 0, and a shorter distance to linearization. However, BFR presents the opposite tendency; suppressed V_y, delayed V_x zero-crossing, and minimal lateral dispersion. In short, BFR is characterized by reduced initial curvature, low-speed linearization, and lateral suppression, indicating that a longitudinal field diminishes the thermally aligned driving to the rear.

In case of BRE based on Fig. 13 (e) and Fig. 15 (e), (j), (o), the surface trajectories in the near-DIZ region ($s = 0 - 2mm$) shows larger start $|V|$ and V_y than in BXX and BFR, while V_x starts as negative but very quick cross of zero and becomes positive. In the transition region ($s = 2 - 5mm$), $V_x > 0$ persists and grows, yielding pronounced lateral spread toward the Steel side, whereas V_y decays mildly so that the trajectory paths remain curved toward the toe. In the rear side of weld pool region ($s = 5 - 9mm$), linearization is delayed, $|V|$ and V_y remain elevated, and V_x approaches to positive. As shown in Fig. 16 (e), contrary to BFR, it is expected that the applied field supplies the steel side direction ***F*** on the weld pool surface and the toe-up but root-down directional ***F***s that reposition the surface-shear path closer to the high temperature region which is under the heat source. Therefore, the thermally aligned rearward driving which is composed of plasma-jet and Marangoni effect sustains V_y, while the $+\boldsymbol{x}$ component of ***F*** rapidly establishes and amplifies $V_x > 0$, producing the steel-side bias and speed retention. Compared with BFR, which exhibits smaller V_y

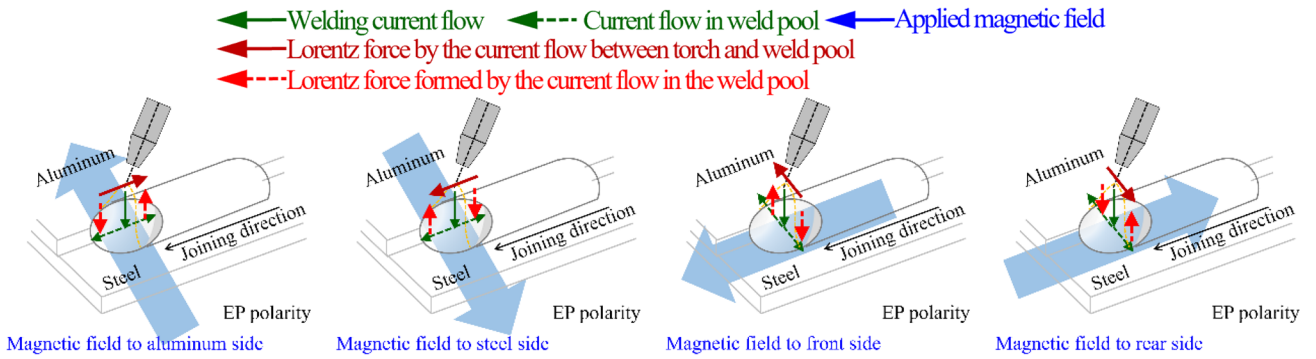

Fig. 16 Schematics of Lorentz force direction in underneath magnetic field applied GMAW

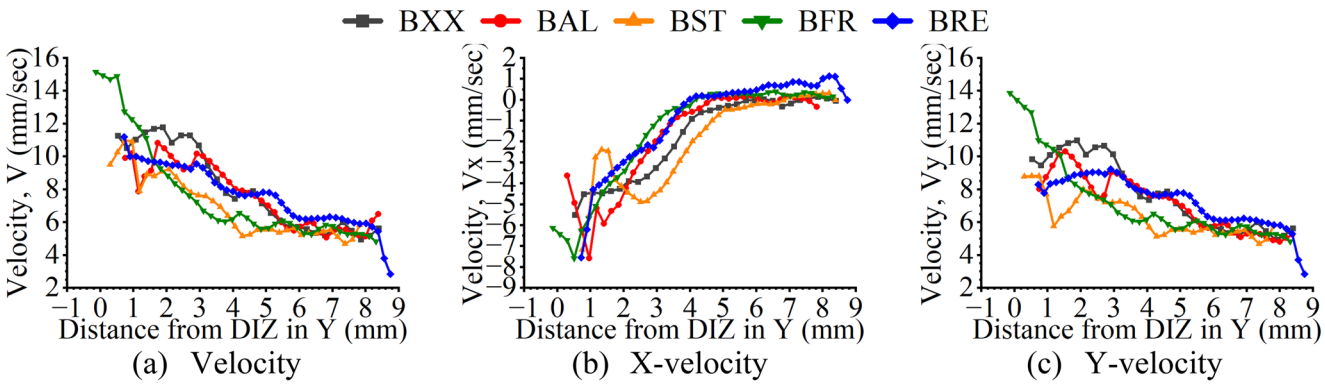

Fig. 17 Average velocity of weld pool center area

with delayed V_x zero-crossing, and early low-speed linearization, BRE features larger initial $\mid V \mid$ and V_y, the fastest growth and saturation of positive V_x, and a longer distance to linearization with higher speeds. Relatively, compared to BXX, BRE consistently shows earlier and stronger steel side bias which is (positive V_x), sustained rearward component, and delayed linearization.

In Fig. 13 (f), averaged DIZ locations in all ***B*** applied conditions formed around that in BXX following their ***F*** direction on the weld pool surface. However, their offset from the DIZ of BXX shows only minor x y offsets. This indicates that the applied magnetic field does not materially shift the droplet impact center due to the strength of Lorentz force which is proportional to the current density and inversely proportional to the distance from the additional underneath magnetic field. Instead, the effect of F controls primarily the redistribution of the heat energy distribution of the heat source on the base metal and the material flow on the weld pool surface, rather than a re-targeting of the droplet landing point.

In short, the droplet path remains effectively pinned, and the observed differences arise from re-weighting of rearward (Y) vs. lateral (X) driving components at the surface.

The overall average velocities at the center region (P2 to P7 in Fig. 13) of the weld pool surface are compared in Fig. 17, and transformed force in the arc heat source by F which is induced by B with its effect are illustrated in Fig. 18, respectively. Taken together Figs. 17 and 18, the mechanism of transformed weld pool surface flow by B is discussed in here.

Figures 17 and 18 show that the additional underneath magnetic field ***B*** interacts with the welding current to generate $F = J \times B$, which tilts the plasma jet as confirmed in 3.1 Arc phenomenon. Since the tilting or bending of arc redistributes current density, and strengthens the surface shear along ***F*** as shown in Fig. 18, thereby setting the direction and magnitude of the weld-pool surface flow. In BAL, a rearward component of ***F*** adds to the intrinsic rearward driving, so V_y is relatively larger while V_x by increased shear forceto the rearward and approaches zero early, producing a rear-dominant and laterally suppressed pattern. In BST, a forward component of ***F*** partially cancels the rearward driving, reducing V_y while maintaining $V_x > 0$, which yields steel-side lateral spread and delayed linearization. In BFR, the longitudinal action of ***F*** gives large $\mid V \mid$ and V_y near the DIZ that decay rapidly to a low-velocity linear

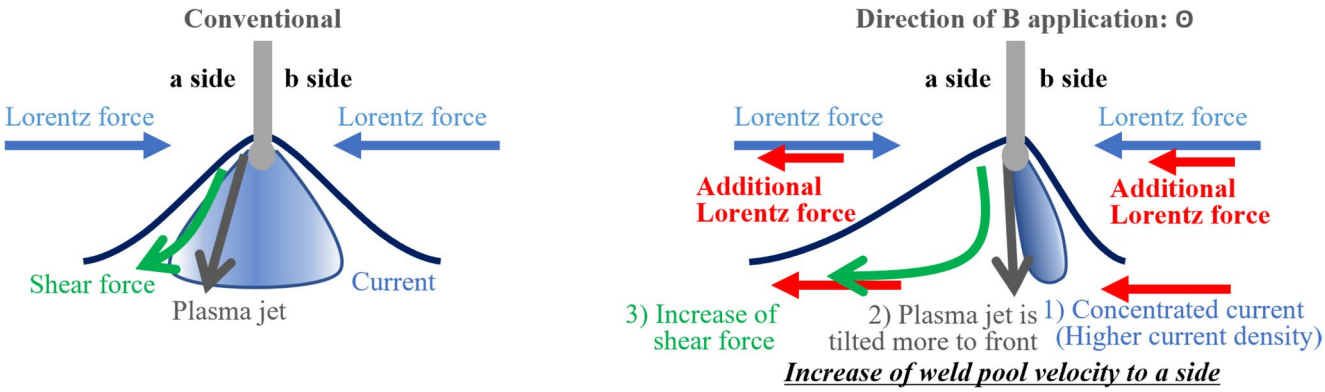

Fig. 18 Mechanism of weld pool flow velocity increase

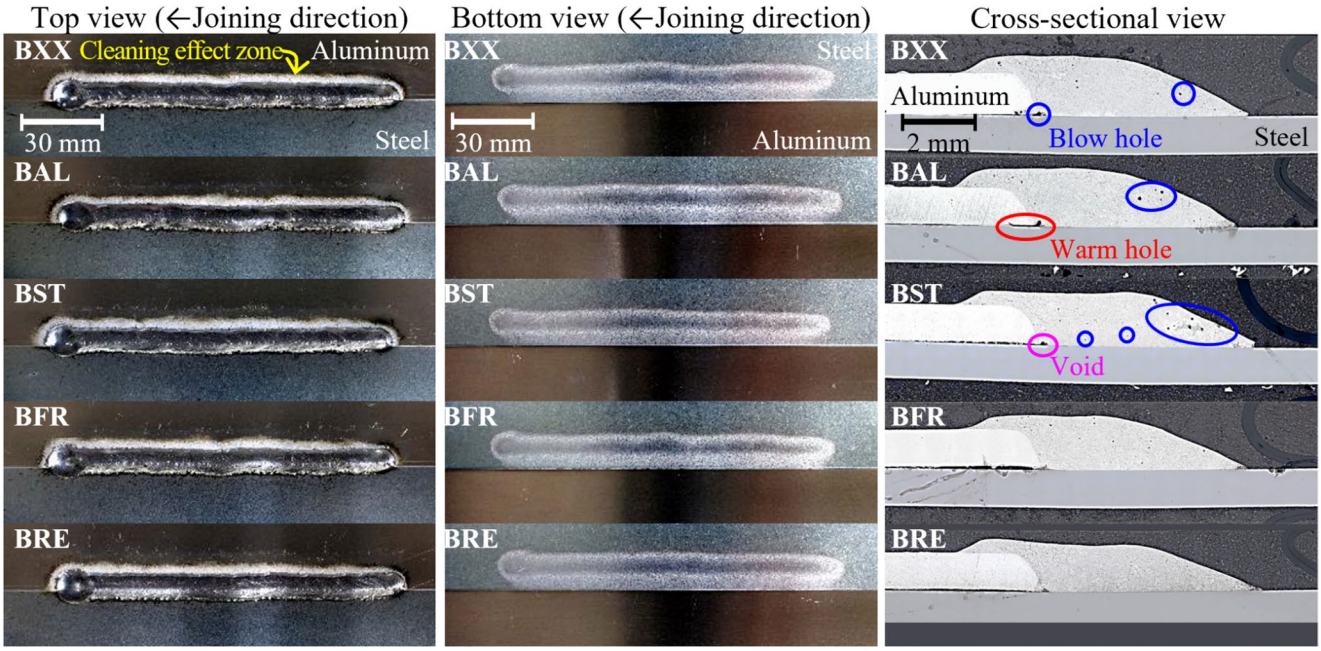

Fig. 19 The bead profiles of the additional magnetic field varied pulse GMAW joints

drift. In BRE, the longitudinal ***F*** directed toward the steel side causes the earliest and strongest rise of positive V_x together with sustained V_y, leading to a pronounced steel-side bias with speed retention. Overall, the orientation of ***B*** re-weights rearward and lateral driving, fixing the initial curvature, the timing of the V_x's zero crossing, the distance to linearization, and the degree of velocity retention are in full agreement with the averaged curves in Fig. 17 and the mechanism sketched in Fig. 18.

3.3 Bead profiles

The top–bottom and cross-sectional bead profiles of joints obtained by ***B*** direction varied pulsed GMAW process are compared in Fig. 19, and corresponding bead dimensions are listed in Table 5, respectively.

It was confirmed that the weld seams obtained in all conditions were fairly smooth, but the aluminum was welded while the steel was brazed due to the gap of melting point. In addition, it was found that the bottom side of the steel was expanded because the Zn layer on its surface was molten or evaporated, due to the heat conduction during the joining process. Especially, it was found that the expanded zone at the bottom side of the steel plate was reached to the edge of the base metal in the ***B*** applied conditions. Compared to BAL, the expansion of steel bottom side in BST showed shallower dimension. Considering the direction of ***F*** in BAL and BST is opposite to each other; ***F*** to rearward in BAL and ***F*** to forward in BST, it can be inferred that the relatively drastic heating of the steel base metal in BAL induced the increased amount of zinc melting or evaporation.

Besides, an Al-Oxide removed cleaning effect zone (CEZ) showing a rough and white-colored region which is located next to the aluminum side joints and after the crater at the joining finish location was observed in all conditions as a result of the clean effect. In here, the cathode spots in EP polarity emit electrons from the oxide film on the surface of the aluminum base metal with high current density. Hence, the aluminum oxide, which has approximately 2345 K of melting point [32], could be removed by the joule heating during joining. Notably, the changes of average CEZ length after the crater and CEZ width next to the bead as

Table 5 Comparison of bead profile dimension

B direction	Cleaning effect zone length after crater (mm)	Cleaning effect zone width (mm)	Bead width (mm)	Wet length (mm)	Bead height (mm)	Wet angle (°)
BXX	2.82	3.57	12.68	9.11	1.7	26
BAL	2.14	3.55	11.38	8.54	2.0	27
BST	4.78	3.62	11.45	8.29	1.84	28
BFR	3.17	4.24	12.45	9.07	2.11	38
BRE	2.99	3.18	12.98	9.88	1.5	22

plotted in Table 5 could be confirmed that their increase or decrease were correspond to the ***F*** direction. In case of the CEZ length, BFR joints and BRE joints showed slightly increased value as 3.17 and 2.99 mm, respectively, compared to BXX joints which formed 2.82 mm. However, BAL joints which had rearward ***F*** and BST joints which had forward ***F*** showed decreased average CEZ length as 2.14 mm and that as 4.78 mm, respectively. Similarly, CEZ width was also increased or decreased by following the ***F*** direction. BXX joints formed 3.57 mm, and BAL and BFR formed 3.55 mm and 3.62 mm in similar, but BFR showed increased to 4.24 mm and BFR showed decreased to 3.18 mm.

Additionally, it was found that the bead dimension was varied by the direction of ***F***. Except BRE joints, the wet length was mostly decreased and the bead height was increased in B applied conditions compared to BXX joints. In BRE joints whose ***F*** direction was to the steel side, the wet length was increased from 9.11 to 9.88 mm, and the bead height and the wet angle were decreased from 1.7 mm to 1.5 mm and from 26 ° to 22 °, respectively, when it was compared to BXX joints.

Different from BXX, the final geometry of ***B*** applied GMAW joints showed unique morphologies. In case of BRE which has longer wet length and lower bead height than BXX, for example, it showed a flat-close shape. Further, the geometry showed the relatively thicker near the toe but thinner root with two humps on the bead top surface. As discussed in 3.1 Arc phenomenon to 3.2 Weld pool surface flow, this shows an agreement that ***F*** in the weld pool which is generated by interaction between ***B*** and the current flow in the weld pool during joining pushes up the molten aluminum near the toe side but pull down the root area to be flat. As referring Fig. 16 which is about the directions of ***F*** under the application of additional magnetic field, the change of bead geometry can be explained. In BRE, mainly three directions of the additional Lorentz force are formed. Around the current flow between the electrode filler wire and base metal, the rear side directional additional magnetic field forms the steel side directional force. Interacting with the current in the weld pool which is from the plasma arc heat source under the low electrical resistance, at the same time, the vertical directional additional Lorentz force is generated. Especially, the current flow in the weld pool from the arc to the root (aluminum) side which is perpendicular to the additional magnetic field, the downward directional Lorentz force is generated and pulls down the weld pool. In contrast, the current flow to the toe (steel) side, which has opposite directional flow compared to the current from to root side, newly generated additional Lorentz force acts as an upward force in here. Consequently, the weld pool of BRE condition experiences the steel side biased arc with downward and upward forces in its root and toe area, respectively, and forms the bead as flatter and wider shape implying the effect of additional Lorentz force direction.

In the cross-sections of all conditions, blow holes were observed, as summarized in Table 6, but their average diameter and area fraction varied depending on the ***B*** direction. In BFR and BRE, the average blow hole diameters were as small as 37 μm (0.037 mm with 0.013 standard deviation) and 23 μm (0.023 mm with 0.007 standard deviation), respectively, and the porosity area fraction in the cross-section was also low (0.339% for BFR and 0.16% for BRE). Therefore, these blow holes are unlikely to act as critical defects that strongly deteriorate the mechanical properties of the joints. In BXX, the average blow-hole diameter was approximately 50 μm (porosity area fraction: 0.45%, standard deviation: 0.03), and a maximum diameter of 0.124 mm was observed at the root. In BAL and BST, blow holes were formed mainly near the toe. However, a relatively upward directional large worm hole and a void with a length of about 1.078 mm and a diameter of about 0.48 mm were also observed at the root of BAL and BST, respectively. Particularly in BST, a larger number of blow holes were found in the lower region of the bead than in BAL. In addition, solidified Zn with a serrated morphology was observed in BST between the deformed aluminum base metal and the steel base metal.

The formation of blow hole, worm hole, and void at the root area is attributed to the evaporation of Zn which composes the coating layer on the GI steel surface. Since the melting (693 K) and boiling (1180 K) point of Zn are lower than that of Al and Fe, the Zn was evaporated drastically with high vapor pressure. However, the root which has structural limitation does not allow the evaporated zinc to be extracted properly with the turbulent flow of weld pool and faster cooling than the toe area by higher heat conductivity. Based on the formation of blow hole and worm hole is mainly because the solidification of the weld is slower than the growth of the porosity, the structural limitation of the root and effect of additional Lorentz force in BAL condition

Table 6 Comparison of defects in the joints

B direction	Blow hole area fraction (%)	Maximum blow hole diameter (mm)	Average blow hole diameter with standard deviation (mm)	Worm hole and void (mm)
BXX	0.451	0.124 at root	0.048 (±0.03)	-
BAL	0.922	0.1 in worm hole	0.051 (±0.027)	Worm hole 1.078 at root
BST	0.418	0.1 as void	0.059 (±0.023)	Void 0.48 at root
BFR	0.339	0.064	0.037 (±0.013)	-
BRE	0.16	0.038	0.023 (±0.007)	-

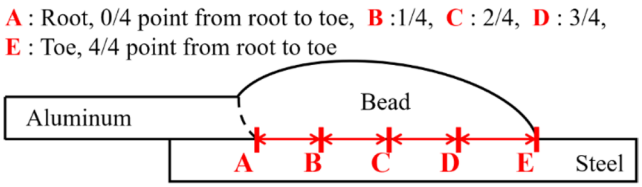

Fig. 20 Measured locations of IMC layer thickness

which leads relatively slower cooling by pushing the arc on the weld pool backwards can explain the frequent formation of the blow hole and worm hole at the root area. In case of BST, it generates the front side directional ***F*** on the weld pool by welding current flow through the arc plasma. Furthermore, the current flow in the weld pool forms the upward additional force at the weld pool front part and that from the rear side generates the downward force at the weld pool rear part during joining, respectively. Thus, the aluminum base metal in BST condition can be heated earlier and smoother than that in the BXX, but it indicates that the following relatively drastic cooling, and the weld pool current induced additional magnetic downward driving force entrapped the evaporated the zinc in the weld pool, so that the zinc moved to the aluminum base metal side and remained as unstable solidification. Additionally, considering about the ***F*** in the rear part of weld pool during BAL is upward, more numbers of blow hole formation at the lower location in the bead by BST is agreed with formation of worm hole in BAL and that of void in BST.

3.4 Formation of Fe-Al IMC layer

Based on the five locations at the joint interface where from root to toe, SEM-EDS analysis was carried out to characterize the Fe-Al intermetallic (IMC) layer distribution at the joint interface. Figure 20 illustrates the investigated locations schematically. Subsequently, Fig. 22 shows the SEM macrographs of the IMC layer at different joining conditions of the additional magnetic field direction varied process. From the top to the bottom in Fig. 22, the obtained SEM macrography of BXX joints, BAL, BST, BFR, and BRE are plotted, respectively. In the plotted SEM macrography, bottom side of the interface indicates steel, while upper side is aluminum alloy. The thickness of the IMC layer was measured at forty locations along the joint interface and their average value and corresponding standard deviation were considered. Corresponding to Fig. 22, the result of EDS spot analysis identifying the element intensity in atomic parentage of Al, Fe, Si and Zn elements along the IMC layer is plotted in Table 7, and the distribution of average IMC layer thickness with standard deviation is compared in Fig. 21, respectively.

Figure 21 shows overall distribution of Fe-Al IMC layer thickness with standard deviation. It was confirmed that the IMC layer thickness was increased drastically in BXX toward the center of the joint but it was decreased drastically again as close to the toe; Location A: approximately 0.67 μm, Location B: 10.06 μm (standard deviation ± 2.88), Location C: 21.71 μm (± 4.33), Location D: 3.77 μm (± 1.17), and Location E: 0.41 μm. Considering the previous study [7] that above than 10 μm of Fe-Al IMC layer can be a critical factor of joint strength deterioration, the thick IMC layer from Location B to somewhere between Location C and D with high standard deviation is associated with lower tensile-shear strength. Especially Location C of BXX which shows significantly thicker layer than other locations, its formation can be explained by the energy distribution of the heat source. In case of the boundary area of the joints such as Location A or E, they get small amount heat energy from the arc plasma which follows the Gaussian energy distribution, but at the center of the joints (Location C), heat energy contained droplet and arc plasma which has much higher energy density than at the joint boundary transfers the heat directly. Thus, IMC whose growth follows temperature variation per unit time could be formed at the center

Table 7 EDS point analysis corresponding to Fig. 22

Point	Al	Fe	Si	Zn	Expected IMC	Point	Al	Fe	Si	Zn	Expected IMC
1	54.2	45.8	-	-	Fe_2Al_5	14	65.1	24.1	3.8	6.9	Fe-Al-Zn
2	67.6	29.5	2.9	-	$FeAl_3$	15	26.1	72.5	0.4	1.0	Fe_2Al_5
3	74.9	25.1	-	-	$FeAl_3$	16	61.6	27.7	0.6	10.1	Fe-Al-Zn
4	51.4	48.6	-	-	FeAl	17	65.4	26.2	0.6	7.9	Fe-Al-Zn
5	72.9	24.5	2.6	-	Fe-Al-Si	18	75.9	24.1	-	-	$FeAl_3$
6	60.0	25.7	7.8	6.4	Fe-Al-Zn	19	70.5	25.5	4.0	-	Fe_2Al_5
7	75.8	23.6	0.2	0.3	$FeAl_3$	20	24.6	73.0	2.3	-	Fe_3Al
8	-	-	-	-	Fe-Al-Si	21	71.0	25.4	3.1	0.5	$FeAl_3$
9	49.1	42.3	8.1	0.4	FeAl	22	42.5	54.0	3.3	0.2	FeAl
10	49.1	46.4.	3.1	1.4	FeAl	23	41.9	58.1	-	-	FeAl
11	69.1	30.4	0.5	-	Fe_2Al_5	24	77.4	-	-	-	$FeAl_3$
12	67.8	32.2	-	-	$FeAl_2$	25	71.6	23.0	5.4	-	$FeAl_3$
13	84.4	-	15.6	-	Al-Si						

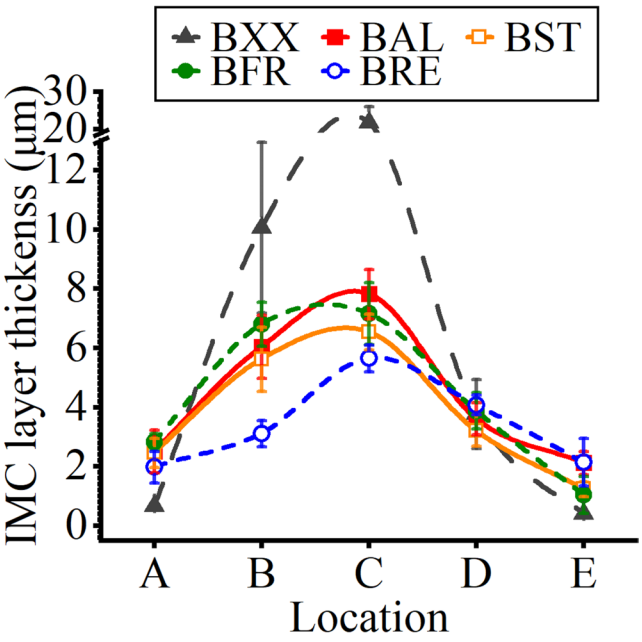

Fig. 21 IMC layer thickness distribution; average layer thickness with standard deviation

with significant thickness. In contrast, all ***B*** applied conditions were confirmed that their maximum average IMC layer thickness was formed in Location C as 7.82 μm (± 0.83), 6.54 μm (± 0.61), 7.17 μm (± 1.04), 5.65 μm (± 0.46) in BAL, BST, BFR, and BRE, respectively, but their thickness are thinner than 10 μm and it can be inferred that joint strength can be improved compared to BXX. Not only the thickness of IMC layer, but also the distribution tendency of the layer was different depending on the B direction, but this will be discussed together with IMC composition together at the end of this chapter.

In all conditions as shown in Fig. 22, the morphology of the Fe-Al IMC layer was a smooth interface between the IMC and the steel, but serrated shaped interface was observed toward the aluminum side due to the non-uniform diffusion of Fe to Al. Furthermore, Fe-Al-Si and Fe-Al-Zn compounds were formed at the boundary of the Fe-Al IMC as similar with other studies [35, 36] which employed conventional GMAW. The intensity of Fe and Al in IMC layer indicates the possible formation of various IMCs. Substituting the atomic percentage value of the Al and Fe elements in into Al-Fe binary phase diagram, it was confirmed that the IMC at the joint interface was mainly composed of Al-rich IMCs such as $FeAl_3$ and Fe_2Al_5 with Fe-Al-Si or Al-Si coverage as shown in Table 7. As the melting temperature of Zn (693 K) is lower than Al (925 K) and Zn as a solute has lower mutual affinity to Al or to Fe than the Al to Fe [37], it can be concluded that the molten Zn at the joint interface was transferred to the root and toe with non-precipitation of liquid Zn to Fe-Al IMC in the middle of the joint during joining. Especially, the middle of the joint where gets the edge directional driving force at the bottom of the weld pool by arc pressure and additional Lorentz force pushed the molten zinc by the edge directional momentum, and by the capillary effect between the liquid Zn and the solid Al during cooling. Contrast to the middle of the joints, Locations A and E in Fig. 23 showed that the Zn contained IMC such as $Fe_2Al_{5-x}Zn_x$ IMC at the joint interface. Considering that Fe-Al-Zn IMC was not attained at Location B because the Zn was evaporated drastically or transferred to the edge of the joint after the dissolution stage, it can be inferred that the transferred liquid Zn was precipitated to Fe_2Al_5 IMC during cooling due to the high affinity of Al to Zn. As known as the Zn contained Fe-Al IMC is significantly more ductile than only Fe-Al IMCs [38], it can be inferred that the IMC distribution at the root and toe which formed lower than the required 10 μm thickness layer with Zn contained composition may not result the brittle cleavage fracture at the joint interface of these area.

BXX condition which is the conventional DC pulse GMAW condition in Fig. 23 shows the average values of the IMC layer thickness in Location A to C increase from 0.67 μm (≈ 1 μm) to 21.71 μm (± 4.33) and decrease again as close to Location E as 3.77 μm (± 1.17) to 0.41 μm (≈ 0 μm). This can be attributed to the ratio of heat energy distribution in GMAW heat source. Moreover, this indicates that the growth of IMC layer is determined by the temperature variation in unit time based on the Fick's second law. BXX shows that the IMC layer in Location A and B formed the thicker layer than that in Location D and E, respectively. This is attributed to the structural limitation induced higher heat conductivity in the root side. A tight set of base metals allows the domination of heat conduction to be stronger in the heat transfer, therefore the root side faces more drastic temperature variation than the toe side faces. Since the growth of Fe-Al IMC layer is following the parabolic law of diffusion as a function of temperature and time [12], the drastic temperature variation in this area finally forms the thicker layer than in the toe area.

Compared to BXX, the ***B*** applied joint showed the significantly decreased thickness of IMC layer due to the decreased heat input by the moving of heat source. The maximum average IMC layer thickness of BXX was attained as 21.71 μm (±4.33) at the Location C, while that of BAL, BST, BFR, and BRE showed 7.82 μm (±0.83), 6.54 μm (±0.61), 7.17 μm (±1.04), and 5.65 μm (±0.46) in Location C, respectively. In pulsed GMAW which cyclically provides a current waveform as a mixture of peak and base current, the application of additional magnetic field results the strong additional Lorentz force in the peak current section, but the lower level of the additional Lorentz force is either generated in the base current section. From this, the

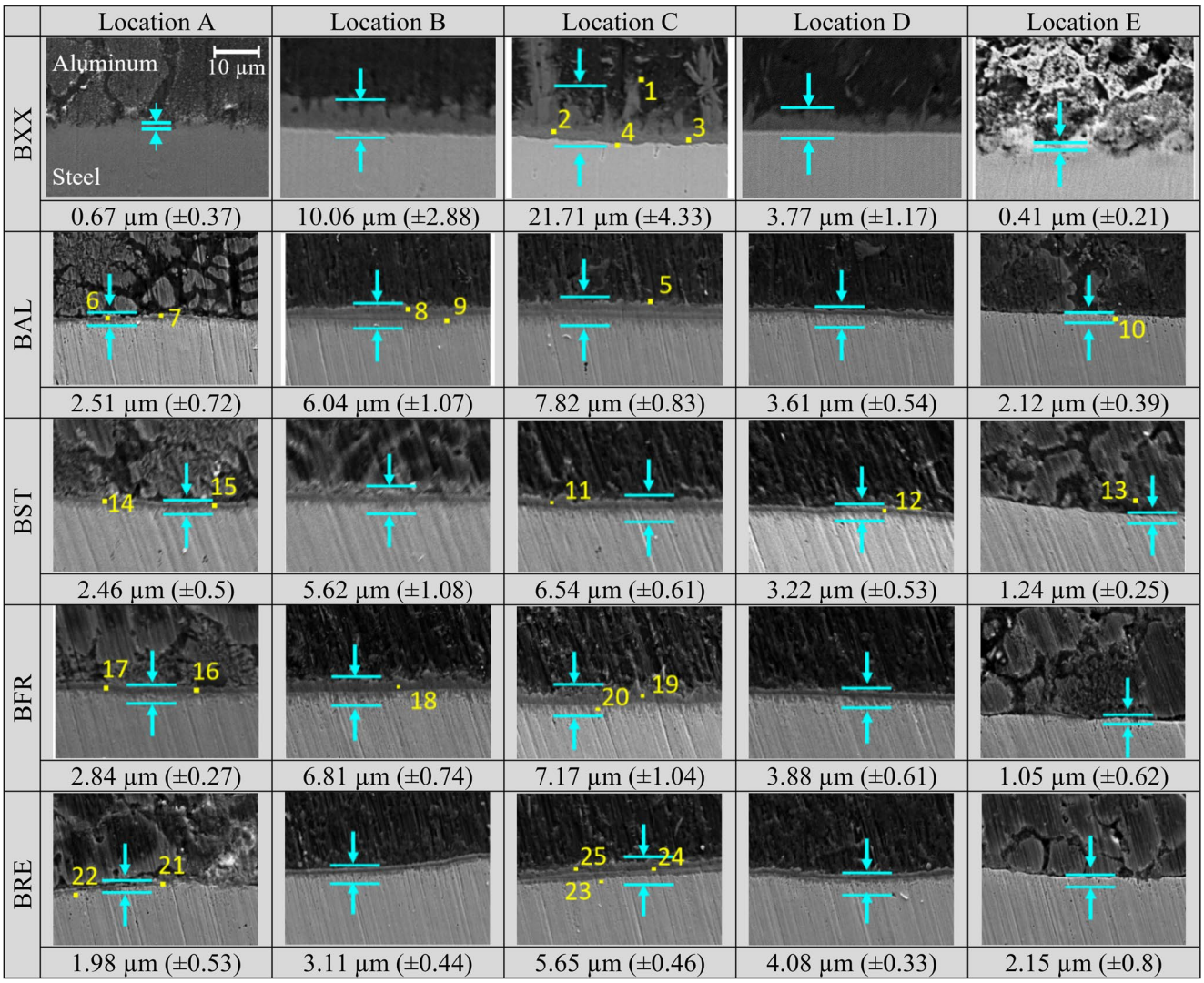

Fig. 22 SEM macrography of IMC layer in the additional magnetic field direction varied DC pulse GMA joints

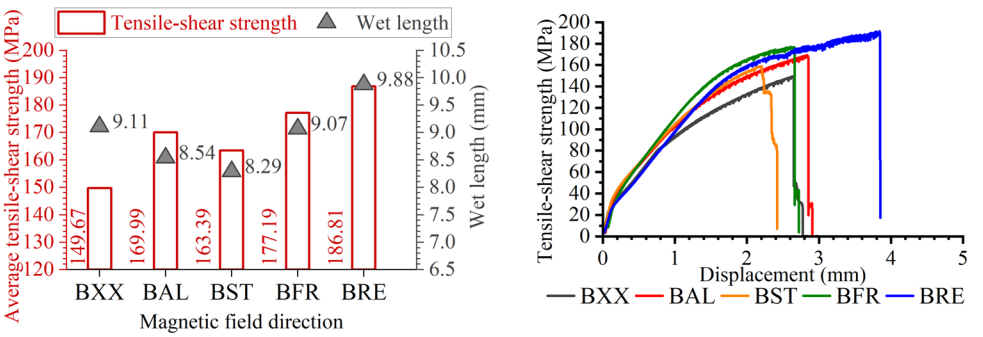

Fig. 23 Comparison of tensile-shear strength

(a) Average tensile-shear strength and wet length

(b) Representative strength-displacement curve

electric arc heat source moves periodically along the varied additional force direction as shown in Fig. 11 in Sect. 3.1 Arc phenomenon, and it distributes the same amount of total heat energy to the wider range of the base metal surface than the heat source in BXX distributes. Although some spots such as Location B and D may get higher heat input compared to BXX condition during joining because the arc moves with the Gaussian heat energy distribution,

Table 8 Tensile-shear strength

Condition	Additional Lorentz force direction	Tensile-shear strength (MPa)			Joint Efficiency (%)
		Minimum	Maximum	Average	
BXX	-	123.9	175.3	149.67	68.0
BAL	to rear side	154.0	182.5	169.99	77.3
BST	to front side	154.3	170.2	163.39	74.3
BFR	to aluminum side	173.6	185.1	177.19	80.5
BRE	to steel side	179.1	190.1	186.81	84.9

the moving heat source provides the decreased amount of heat to the joint area in a given time. Therefore, the additional magnetic field applied joint can achieve the decreased thickness of the IMC layer.

Corresponding to the moving heat source by the ***F***, the distribution of IMC layer thickness in ***B*** applied conditions showed the increase and decrease tendency along the F direction. Referring Figs. 16 and 18 which show the tilting and moving of arc and the direction of the additional Lorentz force generated by the welding current and ***B***, respectively, it can be confirmed that that BAL and BST in Fig. 21 show the similar IMC layer thickness distribution tendency with BXX. However, BAL and BST showed differed IMC layer thickness due to the heat generation at the spots per unit time was changed. Similarly, BFR and BRE showed that their IMC layer distributions have the opposite directional tendency each other because the arc was tilted to the aluminum side and the steel side, respectively. The IMC layer thickness gap between Location B and D in BFR was higher than that in BRE due to the formation of arc in BFR was concentrated at the root area whose heat transfer is more affected by the heat conductivity of base metals than at the toe area. Based on the formation of IMC in a spot is governed by the temperature variation per unit time, therefore, it can be inferred that the drastic temperature variation by the higher heat conductivity at the root allowed the root side biased IMC layer thickness distribution. In contrast, BRE concentrates the arc to the toe side direction whose temperature history can show smoother tendency than the root. Thus, the IMC layer shows toe side biased distribution, but it forms the thinner layer gap between Location B and D due to the smoother temperature variation at the joint interface.

3.5 Mechanical evaluation of the joint

The comparison of tensile-shear strength of the joints is shown in Table 8; Fig. 23 to investigate the effect of joint geometry on the strength. Figure 23 (a) show the average tensile-shear strength with wet length of the bead, and Fig. 23 (b) shows representative curves of strength-displacement curve, respectively. The tensile-shear test was carried out on seven specimens in each condition to secure the mechanical characteristics of the joint.

The maximum average tensile shear strength of the conventional BXX joints was 149.67 MPa, and their joint efficiency was approximately 68% of that of the aluminum base metal (220 MPa). Conspicuously, it was confirmed that applying the additional underneath magnetic field increased the tensile-shear strength; approximately 170.0 MPa in BAL, 163 MPa in BST, 177 MPa in BFR, 187 MPa in BRE, respectively. Especially, the maximum average tensile-shear strength was attained in BRE with approximately 85% joint efficiency as the application of additional Lorentz force expanded the area where the heat source covers and decreased the heat input per unit area to the base metal. This may because the periodical movement of the arc during joining led the expansion of the joining area and the actual input heat to the joint interface was decreased with decrease of IMC layer thickness as confirmed in Fig. 21. Interestingly, in case of BST, it achieved higher tensile shear strength than BXX but failed in lower displacement as shown in Fig. 23 (b).

Corresponding to the tensile-shear strength of the joints in Fig. 23; Table 8; Fig. 24 shows SEM macrography of the fracture surface of the joint to the aluminum side as a result of the tensile-shear test. It was confirmed that BXX joints was failed near or along the fusion line, along the vertical direction of the bead. In case of the maximum average tensile shear strength condition which is BRE, the specimens were mainly failed around the HAZ area showing the fracture surface with mainly the shortest average radius of dimples. All the conditions showed the dimples at the fracture surface implying the ductile fracture, but BXX shows the grain boundary peeled out surface was observed at the same time. This indicates the fracture of BXX joint, which also showed excessive IMC layer thickness at the center of the

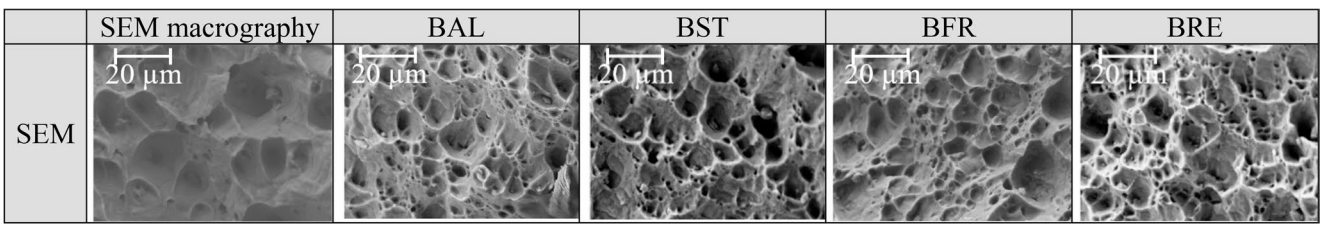

Fig. 24 Comparison of fracture surface of the joints

joint interface, was propagated with both ductile and brittle fractures. Noting that the porosities such as blow hole, warm hole, or void were observed at the root area in BXX, BAL, and BST, respectively, but dimples were mainly observed in all conditions as plotted in Fig. 24, it can be inferred that the porosities at the root area which are formed by the evaporation of Zn worked as notch for stress intensification in the root. Since the joining process in this study does not provide leg length and penetration depth in the joint due to its aluminum welding - steel brazing characteristics, the wet length of the bead was considered as the morphological factor. The result indicated that the change of wet length in Fig. 23 can improve the tensile-shear strength of the joint corroborating with the wet length increased conditions; BFR and BRE shows the increased joint strength. However, it was inferred that the correlation between the wet length and the joint strength has to be treated as an additional factor to guarantee the strength of the joint because the length in BAL and BST were less than BXX and their joint strength was increased slightly compared to their decrease of wet length. Therefore, it can be concluded that the control of the temperature variation of the joint under the given heat input with preventing the possible formation of defect has to be considered as a way of improving tensile-shear strength of dissimilar material joints. Further, it is realized that the application of additional Lorentz force affected significantly to the joint strength in pulse GMAW by controlling the periodical change of heat source direction leading a change of heat energy distribution with physical phenomenon controller to the weld pool.

Consequently, it was found that the application of additional magnetic field to the rear direction can enhance the joint strength by decreasing the heat input to the joint interface, and by suppressing the formation of porosities by controlling of Zn evaporation during joining.

4 Conclusions

In this study, 1.2 mm thick dissimilar AA5052 aluminum alloy and hot-dip galvanized (GI) steel plates were joined by a pulsed GMAW process assisted by an additional underneath magnetic field. The effects of the additional Lorentz force on the arc behavior, weld pool surface flow, formation of the Fe–Al intermetallic compound (IMC) layer, and the resulting mechanical properties of the joints were analyzed. The major conclusions can be summarized as follows:

1) The arc direction, weld-pool surface flow pattern, and corresponding flow velocity varied with the direction of the additional Lorentz force. The additional Lorentz force can be divided into two components depending on the current path: (i) that generated by the welding current flowing between the electrode wire and the base metal, and (ii) that generated by the current flowing in the base metal, especially in the weld pool.
2) Compared with the conventional pulsed GMAW joints, the joints welded with the magnetic field directed toward the rear side exhibited an increased wet length and a reduced bead height. This behavior is attributed to the Lorentz force generated by the welding current, which deflects the arc toward the steel side and promotes spreading of the molten aluminum. In addition, the magnetic field associated with the current flowing in the weld pool deforms the bead top surface, acting as an upward driving force in the toe region (steel side) and a downward driving force in the root region (aluminum side).
3) When the Lorentz-force direction was oriented along the joining line rather than perpendicular to it, blow holes and worm holes were more frequently formed owing to more drastic solidification caused by a Lorentz-force-induced arc tilt and by upward and downward weld-pool flow at the rear part of the weld pool, respectively. The root region has higher heat conductivity than the toe, solidification proceeds more rapidly and the evaporated Zn is more easily trapped, leading to concentrated porosity at the root.
4) Compared with the average IMC layer thickness in conventional pulsed GMAW joints, the additional underneath magnetic field assisted pulsed GMAW process produced a significantly thinner Fe–Al IMC layer. This reduction is attributed to decreased local heat generation at the joint interface, because the periodically displaced arc distributes a given total heat input over a wider area than in the conventional condition. These results indicate that the rate of heat input per unit length at the joint interface strongly governs the growth of the Fe–Al IMC layer.
5) The highest average tensile-shear strength, 186.81 MPa (approximately 85% joint efficiency), was obtained under the magnetic field to rear side condition, which also exhibited an increased wet length. This improvement is ascribed to the combined effects of reduced heat input and increased wet length when the additional Lorentz force is directed toward the steel side. The fracture mode under this optimum condition was predominantly ductile, propagating from near the fusion line along the thickness direction of the weld.

Overall, it was confirmed that applying an underneath magnetic field toward the rear side during pulsed GMAW improves the joint quality of AA5052 aluminum alloy–GI steel lap joints. The improved joint quality was evidenced

by decreased effective heat input, suppressed defect formation with increased wet length, and suppressed Fe–Al IMC layer growth, which collectively led to an increased tensile-shear strength. From a configuration standpoint, the underneath approach adopted in this study applies a modest magnetic flux density on the order of 1 mT at the workpiece surface. This differs from under-torch (around-torch) magnetic strategies, which can directly interact with the arc column and often require modifications near the torch. In contrast, the present coil-in-fixture arrangement can be implemented beneath the workpiece and is compatible with simple clamping for thin Al/steel lap joints. Therefore, these results can suggest a feasible route for integrating magnetic-field assistance into automotive and aerospace production lines where stable and improved joint strength is required for thin parts. In addition, the present findings may motivate future research to further control heat input and magnetic flux density together with joint geometry and Zn distribution when joining aluminum alloys to Zn-coated steel using pulsed GMAW, or delineate an industrial process window by optimizing magnetic flux density and duty cycle, while evaluating long-term robustness, cost, and cycle-time impacts for practical implementation.

Acknowledgements This work was supported by JSPS KAKENHI Grant Number JP24954231, the Project on Design & Engineering by Joint Inverse Innovation for Materials Architecture (DEJI2MA) from the Ministry of Education, Culture, Sports, Science and Technology (MEXT), an OU Master Plan Implementation Project promoted under Osaka University.

Author contributions Seong Min HONG: investigation, visualization, writing–original draft preparation. Shinichi TASHIRO: resource, review and editing. Hee-Seon BANG: resources, validation. Kenta YAMANAKA: resources, validation. Manabu TANAKA: validation, supervision. Kazuhiro ITO: validation, supervision.

Funding Open Access funding provided by The University of Osaka

Declarations

Ethical approval The authors state that the present work is in compliance with the ethical standards.

Consent to participate All the authors listed have approved the manuscript and consented to participate.

Consent for publication All the authors listed have approved the manuscript and consented for publication.

Conflict of interest The authors declare no competing interests.

References

1. Tanaka K, Shigeta M, Tanaka M, Murphy AB (2019) Investigation of the bilayer region of metal vapor in a helium tungsten inert gas Arc plasma on stainless steel by imaging spectroscopy. J Phys D 52(35):354003
2. Song JL, Lin SB, Yang CL, Fan CL, Ma GC (2010) Analysis of intermetallic layer in dissimilar TIG welding–brazing butt joint of aluminium alloy to stainless steel. Sci Technol Weld Joining 15(3):213–218
3. Xiao L, Fan D, Huang J (2018) Tungsten cathode-arc plasma-weld pool interaction in the magnetically rotated or deflected gas tungsten Arc welding configuration. J Manuf Process 32:127–137
4. Dong H, Hu W, Duan Y, Wang X, Dong C (2012) Dissimilar metal joining of aluminum alloy to galvanized steel with Al–Si, Al–Cu, Al–Si–Cu and Zn–Al filler wires. J Mater Process Technol 212(2):458–464
5. Coelho RS, Kostka A, Dos Santos JF, Kaysser-Pyzalla A (2012) Friction-stir dissimilar welding of aluminium alloy to high strength steels: mechanical properties and their relation to microstructure. Mater Sci Engineering: A 556:175–183
6. Shahverdi HR, Ghomashchi MR, Shabestari S, Hejazi J (2002) Microstructural analysis of interfacial reaction between molten aluminium and solid iron. J Mater Process Technol 124(3):345–352
7. Schubert E, Zerner I, Sepold G (1997, August) Laser beam joining of material combinations for automotive applications. Lasers in material processing, vol 3097. International Society for Optics and Photonics, pp 212–221
8. Pouranvari M (2017) Critical assessment 27: dissimilar resistance spot welding of aluminium/steel: challenges and opportunities. Mater Sci Technol 33(15):1705–1712
9. Su Y, Hua X, Wu Y, Zhang Y, Guo Y (2015) Characterization of intermetallics layer thickness at aluminum–steel interface during overlaying. Mater Design 78:1–4
10. Wang T, Sidhar H, Mishra RS, Hovanski Y, Upadhyay P, Carlson B (2019) Evaluation of intermetallics layer at aluminum/steel interface joined by friction stir scribe technology. Mater Design 174:107795
11. Das A, Shome M, Goecke SF, De A (2016) Numerical modelling of gas metal Arc joining of aluminium alloy and galvanised steels in lap joint configuration. Sci Technol Weld Joining 21(4):303–309
12. Goecke SF, Makwana P, Shome M, De A (2019) Probing joint strength and distortion in gas metal Arc lap joining of aluminum and steel sheets. Weld World 63(2):229–236
13. Gatzen M, Woizeschke P, Radel T, Thomy C, Vollertsen F (2017) Experimental and numerical investigation of an overheated aluminum droplet wetting a Zinc-Coated steel surface. Metals 7(12):535
14. Hong SM, Tashiro S, Bang HS, Tanaka M (2021) Numerical analysis of the effect of heat loss by zinc evaporation on

aluminum alloy to hot-dip galvanized steel joints by electrode negative Polarity ratio varied AC pulse gas metal Arc welding. J Manuf Process 69:671–683
15. Windmann M, Röttger A, Kügler H, Theisen W, Vollertsen F (2015) Laser beam welding of aluminum to Al-base coated high-strength steel 22MnB5. J Mater Process Technol 217:88–95
16. Sierra G, Peyre P, Beaume FD, Stuart D, Fras G (2008) Steel to aluminium braze welding by laser process with Al–12Si filler wire. Sci Technol Weld Joining 13(5):430–437
17. Nomura K, Morisaki K, Hirata Y (2009) Magnetic control of Arc plasma and its modelling. Weld World 53(7):R181–R187
18. Nomura K, Ogino Y, Hirata Y (2012) Shape control of TIG Arc plasma by cusp-type magnetic field with permanent magnet. Weld Int 26(10):759–764
19. Yin X, Gou J, Zhang J, Sun J (2012) Numerical study of Arc plasmas and weld pools for GTAW with applied axial magnetic fields. J Phys D 45(28):285203
20. Wang QW, Zhu S, Yin FL, Liang YY, Wang XM (2012) Numerical simulation of MIG welding Arc with longitudinal magnetic field. Materials science forum, vol 704. Trans Tech Publications Ltd, pp 668–673
21. Matsumoto N, Kuno I, Yamamoto T, Sugimoto M, Takeda K (2012) Arc behavior in non-uniform AC magnetic field. ISIJ Int 52(3):488–492
22. Espina-Herna´ ndez JH, Caleyo F, Hallen JM, Rueda-Morales GL, Pe´ rez-Baruch E, Lo´ pez-Montenegro A (2010), January Method to reduce arc blow during DC arc welding of pipelines. In International Pipeline Conference (Vol. 44229, pp. 387–392)
23. Lu L, Chang YL, Li YM, Gao F (2013) Mechanism analysis of magnetic control high-speed welding undercuts disappear. In Advanced Materials Research (Vol. 774, pp. 1127–1131). Trans Tech Publications Ltd
24. Zhen LI, Lan PENG, Li YR (2014) Effects of geometric parameters and axial magnetic field on buoyant-thermocapillary convection during detached solidification. Trans Nonferrous Met Soc China 24(5):1512–1520
25. Dennis BH, Dulikravich GS (2001) Magnetic field suppression of melt flow in crystal growth. In CHT'01-Advances in Computational Heat Transfer II. Proceedings of a Second Symposium. Begel House Inc
26. Li Y, Luo Z, Yan F, Duan R, Yao Q (2014) Effect of external magnetic field on resistance spot welds of aluminum alloy. Mater Design 56:1025–1033 (1980–2015
27. Lim YC, Yu X, Cho JH, Sosa J, Farson DF, Babu SS, Flesner B (2010) Effect of magnetic stirring on grain structure refinement part 2–Nickel alloy weld overlays. Sci Technol Weld Joining 15(5):400–406
28. Chang YL, Liu XL, Lu L, Babkin AS, Lee BY, Gao F (2014) Impacts of external longitudinal magnetic field on arc plasma and droplet during short-circuit GMAW. The International Journal of Advanced Manufacturing Technology, 70(9–12), 1543–1553
29. Hong SM, Tashiro S, Bang HS, Tanaka M (2021) A Study on the Effect of Current Waveform on Intermetallics Formation and the Weldability of Dissimilar Materials Welded Joints (AA5052 Alloy—GI Steel) in AC Pulse GMAW. Metals, 11(4), 561. Miki. S. Research on application of MIG welding to aluminum alloy die-cast materials and reduction of blowholes (Master thesis). Osaka University, Osaka, Japan (In Japanese)
30. Tanaka M (2014) Plasma diagnostics of Arc during MIG welding of aluminum. Materials science forum, vol 783. Trans Tech Publications Ltd, pp 2828–2832
31. Tashiro S, Mamat SB, Murphy AB, Yuji T, Tanaka M (2022) Numerical analysis of metal transfer process in plasma MIG welding. Metals 12(2):326
32. Faugeras O (1993) Three-dimensional computer vision: a geometric viewpoint. MIT Press
33. Faig IW (1975) Calibration of close range photogarmmetric system: mathematical formulation. Photogrammetric Eng Remote Sens 41(12):1479–1486
34. Tashiro S, Van Bui H, Suga T, Sato T, Tanaka M (2019) Investigating cathode spot behavior in argon alternating current tungsten inert gas welding of aluminum through experimental observation. J Phys D 52(26):26LT02
35. Kobayashi S, Yakou T (2002) Control of intermetallics layers at interface between steel and aluminum by diffusion-treatment. Mater Sci Engineering: A 338(1–2):44–53
36. Su J, Yang J, Li Y, Yu Z, Chen J, Zhao W, Tan C (2020) Microstructure and mechanical properties of laser fusion welded Al/steel joints using a Zn-based filler wire. Optics & Laser Technol 122: 105882
37. Cox RG (1986) The dynamics of the spreading of liquids on a solid surface. Part 2. Surfactants. J Fluid Mech 168:195–220
38. Dharmendra C, Rao KP, Wilden J, Reich S (2011) Study on laser welding–brazing of zinc coated steel to aluminum alloy with a zinc based filler. Mater Sci Engineering: A 528(3):1497–1503